Performance of solar-sail materials at the photo-gravitational equilibrium point (Formula presented)

ARTICLE IN PRESS

Available online at www.sciencedirect.com

ScienceDirect

Advances in Space Research xxx (xxxx) xxx

ADVANCES IN SPACE RESEARCH (a COSPAR publication)

www.elsevier.com/locate/asr

Performance of solar-sail materials at the photo-gravitational equilibrium point L_1 ☆

Marina Coco [a,*], Catello Leonardo Matonti [a,*], Giuseppe Governale [a], Elena Ancona [b], Roman Ya. Kezerashvili [c]

[a] *Department of Mechanical and Aerospace Engineering, Politecnico di Torino, Corso Duca degli Abruzzi, 24, Turin 10129, Italy*

[b] *Department of Mechanics, Mathematics & Management, Politecnico di Bari, Bari 70126, Italy*

[c] *New York City College of Technology, CUNY, Long Island University, Brooklyn, NY 11201, USA*

Received 20 December 2025; received in revised form 8 June 2026; accepted 10 June 2026

Abstract

This research investigates the performance of solar-sail satellite materials, focusing on their optical and mechanical resilience under space conditions near the photo-gravitational L_1 point of the Sun-Earth/Moon's System Center of Mass, within the framework of the Photo-gravitational Circular Restricted Three Body Problem. At L_1, solar-sails are exposed to continuous sunlight, intense UV and gamma radiation, and solar particles, all of which can degrade optical and mechanical properties. Results show how this degradation leads to a variation in the optical properties of solar-sail materials, resulting in a displacement from the equilibrium point. This study is motivated by the needs of the Planetary Sunshade System program, a space-based solar geoengineering concept relying on the long-term station-keeping of a swarm of solar-sail satellites.

Keywords: Solar-sail; Space material degradation; Photo-gravitational L_1; Planetary sunshade system

1. Introduction

Solar-sail propulsion has emerged as a viable solution for long-duration, low-thrust space missions. The fact that electromagnetic radiation exerts a pressure upon any surface exposed to it was predicted theoretically by James Clerk Maxwell (Maxwell, 1865; Maxwell, 1873). The experimental discovery of the Solar Radiation Pressure (SRP) was announced at the World Physics Congress by Lebedev (Lebedev, 1901) in Paris in 1900, and became the first quantitative confirmation of Maxwell's theory of electromagnetism. Later, it was also proven experimentally by Nichols and Hull from Dartmouth College (Nichols and Hull, 1903). Yakov Perelman in 1915 in his book Interplanetary Journeys (Perelman, 1915) proposed that SRP could be used for the propulsion of spacecraft. However, he came to the conclusion that it is unrealistic because the SRP is too small. The concept of solar sailing dates back to the early visions of Tsiolkovsky and Tsander in the 1920s (Tsiolkovsky, 1921). Fridrikh Tsander suggested and developed the theoretical concepts of solar sailing (Tsander, 1967; Tsander, 1977). Since then, several studies and demonstrator missions have been developed to exploit SRP as a source of continuous, propellant-free thrust, enabling new opportunities for deep-space exploration

☆ This article is part of a special issue entitled: 'SI: Space Sailing' published in Advances in Space Research.

* Corresponding authors.

E-mail addresses: marina.coco@polito.it (M. Coco), catello.matonti@polito.it (C.L. Matonti), giuseppe.governale@polito.it (G. Governale), elena.ancona@poliba.it (E. Ancona), rkezerashvili@citytech.cuny.edu (R.Ya. Kezerashvili).

https://doi.org/10.1016/j.asr.2026.06.036

0273-1177/

and orbital configurations, such as families of highly non-Keplerian orbits for telecommunications, polar region observation, space-weather monitoring, and solar geoengineering, as reviewed in (McKay et al., 2011). In theory, a Solar-Sail Satellite (SSS) offers an unlimited form of propulsion. In practice, however, its long-term performance is limited by optical degradation and possible loss of structural integrity under prolonged exposure to the harsh space environment. The interaction with ultraviolet radiation, high-energy particles, and micrometeoroids alters the optical properties of the surface (Kezerashvili, 2014), resulting in an increase in the sail's equilibrium temperature. These effects lead to a gradual loss of thrust and, consequently, deviations from nominal trajectories, potentially compromising long-term orbital stability. For this reason, degradation of the sail's optical properties must be properly modeled and accounted for in mission design, particularly for long-duration missions (Edwards et al., 2004b), where the cumulative radiation dose significantly modifies the effective thrust profile. Despite several theoretical investigations (Vulpetti and Scaglione, 1999; Edwards et al., 2004b; Prosvirikov et al., 2006; Edwards et al., 2006; Edwards et al., 2002; Lichodziejewski et al., 2004), a gap still exists between experimental characterization and realistic in-orbit degradation data, motivating the development of analytical models to estimate the impact of degradation on sail performance. In this context, Dachwald and co-authors (Dachwald et al., 2005) introduced a parametric model to describe the evolution of a sail's optical coefficients as a function of the accumulated radiation dose, enabling preliminary assessment of its impact on trajectory and attitude control. The model has been further refined and validated in later studies. Mengali et al. (Mengali et al., 2007) introduced the dependence of the sail material thermo-optical characteristics on constituent and geometrical factors using experimental data. McInnes (McInnes, 2014) derived an approximate closed-form solution for spiral trajectories accounting for time-dependent sail degradation, showing that degradation imposes asymptotic limits on motion. This work was further extended by Bassetto et al. (Bassetto et al., 2020) obtaining a closed-form solution for the heliocentric motion of a Sun-facing SSS with degradation, while Niccolai et al. (Niccolai et al., 2022) extended these results using asymptotic expansion techniques to approximate two-dimensional heliocentric dynamics under continuous optical degradation. More recently, Rozhkov et al. (Rozhkov et al., 2021) extended the classical non-ideal sail models by introducing multilayer film structures, emphasizing that the optical properties play a critical role in spacecraft motion control, particularly in long-term mission scenarios, and that non-perfect reflection, degradation, and temperature dependence must be jointly modeled to capture realistic sail performance. Huang et al. (Huang et al., 2021a) demonstrated that neglecting degradation can lead to a loss of control authority or even orbit divergence, motivating the use of integrated guidance and control schemes with online parameter estimation of the optical coefficients. Most recently, Klein et al. (2026) investigated the degradation of aluminized solar sail membranes due to hydrogen blistering induced by solar wind proton irradiation across several temperature conditions (five irradiated samples) and developed a semi-empirical model to describe the process.

The present study refines the optical degradation model by incorporating multiple degradation sources, grounded on available experimental data, and applies the resulting framework to investigate the dynamics of non-Keplerian orbits within the Photo-gravitational Circular Restricted Three Body Problem (CR3BP), hereafter referenced PCR3BP. By allowing the reflectivity coefficient to vary with time, the study evaluates how degradation leads to a displacement from the equilibrium point. Understanding these coupled effects between material degradation and dynamical behavior is essential for the design of future long-duration SSS missions relying only on SRP as a means of propulsion. In particular, here the SSS mission is considered within the framework of a Planetary Sunshade System, a space-based solar geoengineering concept aimed at mitigating climate change by partially reducing the incoming electromagnetic part of solar radiation. The program envisions deploying a swarm of SSS around the Sun—Earth/Moon Center of Mass (CoM) system, hereafter called $\odot - \oplus\rightmoon$, Lagrange point L_1 to cast a partial shadow on Earth over an extended period (Coco et al., 2025). The findings presented here provide new insights and quantitative tools to support the design and stability assessment of such missions.

The remainder of this paper is organized as follows. Section 2 outlines the dynamical framework employed in our analysis. Section 3 describes the optical and thermal degradation behavior of the sail materials under prolonged solar exposure, employing an exponential model to characterize these effects. Section 4 introduces the Planetary Sunshade System, which serves as the reference application for this work. Section 5 presents the simulation results and discusses their implications. Finally, Section 6 concludes the paper by summarizing the key findings and identifying directions for future research and technology development.

2. Astrodynamics of a SSS in the PCR3BP model

The PCR3BP is adopted in this work as a simplified model to investigate the dynamics of SSS orbits applied to the Sun-Earth-Moon system. Specifically, the two primary bodies, i.e., Sun and Earth/Moon's system CoM, are modeled as point masses located at their respective CoM, with masses $m_{\odot,\oplus\rightmoon}$[1] such that $m_{\oplus\rightmoon} = m_{\oplus} + m_{\rightmoon}$[2]. A constant distance L is assumed between them, which corre-

[1] we will use the comma in the subscript or superscript to indicate that the expression applies separately to each of the variables before and after the comma.

[2] which are equal to $m_{\odot} = 1.9884 \times 10^{30}$ kg, $m_{\oplus} = 5.9722 \times 10^{24}$ kg and kg.

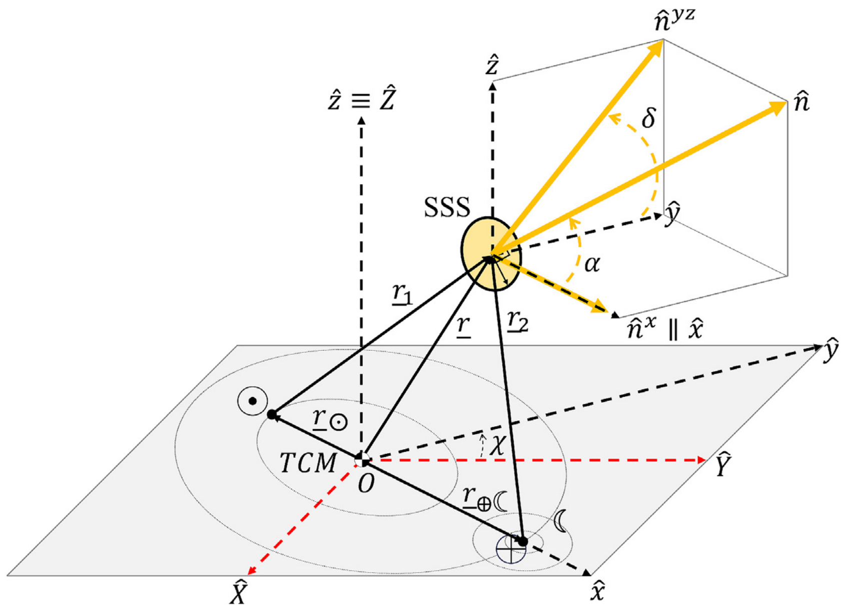

Fig. 1. Illustration of a Solar-Sail Satellite orientation parameters with respect to the corotating S-CCS and the inertial I-CCS: cone angle α and clock angle δ.

sponds to one astronomical unit (AU)[3]. The primaries move along circular orbits around their common Total Center of Mass (TCM) (Ross et al., 2022) with orbital period T [4]. In our work, the values of primaries' masses and orbital parameters are adopted as in (Williams, 2024). Within this model, each SSS is subject to the gravitational attraction of both primaries and to the effect of SRP.

2.1. Equations of motion

In order to obtain the equations of motion of a SSS in the PCR3BP dynamics, it is useful to consider first an Inertial Cartesian Coordinate System (I-CCS) defined as follows: its origin O is located at TCM; its first axis $\widehat{X}$ coincides with the straight line joining the two primaries, from Sun toward Earth/Moon's system CoM, at initial instant t_0 [5]; its third axis $\widehat{Z}$ is along the angular momentum vector of the primaries' system; finally, its second axis $\widehat{Y}$ completes the right-hand I-CCS, such that $\widehat{Y} = \widehat{Z} \times \widehat{X}$. Moreover, it is defined a barycentric Synodic (or co-rotating) Cartesian Coordinate System (S-CCS) where the equations of motion will be written with respect to. This S-CCS is defined as follows: its origin coincides with O which is assumed to be fixed in an inertial frame; its first axis is the rotating straight line joining the primaries (identified by the unit vector $\hat{x} = \cos(\chi)\widehat{X} + \sin(\chi)\widehat{Y}$ with χ as the rotation angle; its third axis $\hat{z}$ coincides with $\widehat{Z}$; finally, its second axis $\hat{y}$ completes the right-hand S-CCS, such that $\hat{y} = \hat{z} \times \hat{x} = -\sin(\chi)\widehat{X} + \cos(\chi)\widehat{Y}$ (see also Fig. 1). Indeed, S-CCS rotates, with respect to I-CCS, around the common third axis with angular velocity equal to Sun-Earth/Moon's system CoM constant mean motion in I-CCS n equal to

$$\mathrm{n} = \frac{2\pi}{T} = \sqrt{\frac{G(m_\odot + m_{\oplus☽})}{L^3}} = 1.9913 \times 10^{-7}\ \text{rad/s} = 2\pi\ \text{rad/year}, \tag{1}$$

with G as the Newton's universal gravitational constant[6] and the rotation angle χ defined as

$$\chi = \mathrm{n}(t - t_0). \tag{2}$$

where t is the time variable. In this study, the equations of motion are rendered dimensionless using the characteristic parameters of Sun-Earth/Moon's system CoM Keplerian circular orbit, namely the distance L and scaled orbital period $\frac{T}{2\pi} = \frac{1}{\mathrm{n}}$.

Moreover, in general, the components matrix in S-CCS are calculated as

$$\boldsymbol{v} = \underline{v} \cdot \begin{Bmatrix} \hat{x} \\ \hat{y} \\ \hat{z} \end{Bmatrix} = \begin{bmatrix} v^x \\ v^y \\ v^z \end{bmatrix}, \tag{3}$$

where $\underline{v}$ is a generic vector and the apex x, y, z are used to indicate its components matrix in S-CCS. Its norm $\|\underline{v}\|$ is then indicated as

$$\|\underline{v}\| = \sqrt{(v^x)^2 + (v^y)^2 + (v^z)^2}. \tag{4}$$

Let us now define the non-dimensional vectors (see also Fig. 1)

[3] which is equal to 1 AU= 1.4960×10^8 km.
[4] which is equal to $T = 1$ year.
[5] we will use the hat symbol ($\hat{\ }$) to indicate a unit vector.
[6] which is equal to $G = 6.6743 \times 10^{-11}$ m^3/kg/s^2.

- $\underline{r}_{\odot,\oplus\rangle}$[7]: position vector of Sun-Earth/Moon's system CoM with respect to O;
- $\underline{r}$: position vector of the SSS with respect to O;
- $\underline{r}_{1,2}$: position vector of the SSS with respect to Sun-Earth/Moon's system CoM, given by

$$\underline{r}_{1,2} = \underline{r} - \underline{r}_{\odot,\oplus\rangle}; \tag{5}$$

- $\underline{a}$: acceleration vector acting on the SSS due to SRP;
- $\hat{n}$: unit vector normal to the sail surface.

The positions of Sun, and Earth/Moon's system CoM are fixed in the synodic (S-CCS) frame, located along the $\hat{x}$ axis. Their components matrices in S-CCS are given by

$$\boldsymbol{r}_\odot = \begin{bmatrix} -\mu \\ 0 \\ 0 \end{bmatrix}, \quad \boldsymbol{r}_{\oplus\rangle} = \begin{bmatrix} 1-\mu \\ 0 \\ 0 \end{bmatrix}, \tag{6}$$

where the dimensionless gravitational parameter μ is defined as

$$\mu = \frac{m_{\oplus\rangle}}{m_\odot + m_{\oplus\rangle}} = 3.0405 \times 10^{-6}. \tag{7}$$

The components matrices in S-CCS of the other position vectors are

$$\boldsymbol{r} = \begin{bmatrix} x \\ y \\ z \end{bmatrix}, \quad \boldsymbol{r}_1 = \begin{bmatrix} x+\mu \\ y \\ z \end{bmatrix}, \quad \boldsymbol{r}_2 = \begin{bmatrix} x-1+\mu \\ y \\ z \end{bmatrix}, \tag{8}$$

while the non-dimensional equations of motion describing the orbital dynamics of a SSS in the S-CCS are (see, for instance Szebehely, 1967; McInnes, 1999)

$$\begin{aligned} \ddot{x} - 2\dot{y} - U_x &= a^x, \\ \ddot{y} + 2\dot{x} - U_y &= a^y, \\ \ddot{z} - U_z &= a^z, \end{aligned} \tag{9}$$

where U indicates the conservative potential

$$U = \frac{1}{2}\left(x^2 + y^2\right) + \frac{1-\mu}{\|\underline{r}_1\|} + \frac{\mu}{\|\underline{r}_2\|}, \tag{10}$$

while the $U_{x,y,z}$ [8] compose the components matrix in S-CCS of $\underline{\nabla U}$ as

$$\nabla \boldsymbol{U} = \begin{bmatrix} U_x \\ U_y \\ U_z \end{bmatrix}, \tag{11}$$

and their expression is reported in extenso in App. A.2.

2.2. Solar radiation pressure

First, we can write the components matrix in S-CCS of $\hat{n}$ as

$$\hat{\boldsymbol{n}} = \begin{bmatrix} \cos(\alpha) \\ \sin(\alpha)\cos(\delta) \\ \sin(\alpha)\sin(\delta) \end{bmatrix}, \tag{12}$$

where the cone angle $\alpha \in I^\alpha = [0, \pi]$ is defined as the angle between $\hat{n}$ and $\hat{x}$, while the clock angle $\delta \in I^\delta = [-\pi, \pi)$ is defined as the angle between the projection of $\hat{n}$ on the plane $\hat{y} - \hat{z}$ and the direction $\hat{y}$ (see also Fig. 1).

By considering a perfectly reflecting surface, the expression for the SRP acceleration vector is assumed to be (see also (McInnes, 1999))

$$\underline{a} = \beta \frac{1-\mu}{\|\underline{r}_1\|^2} (\hat{n} \cdot \hat{r}_1)^2 \hat{n}, \tag{13}$$

where

$$\beta = \frac{\sigma^*}{\sigma}, \quad \sigma = \frac{M}{A}, \quad \sigma^* = \frac{L_\odot}{2\pi G m_\odot c} = 1531.1 \quad \text{kg/km}^2 \tag{14}$$

and A and M as the area and the mass of the SSS, respectively, while σ is the areal mass density and σ^* is the critical sail loading parameter (McInnes, 1999), with $L_\odot$ solar luminosity [9], and c the speed of light [10]. Moreover, since the SRP is the force produced by the light photons impinging on the surface of the satellite, the condition $\hat{n} \cdot \hat{r}_1 = \cos(\alpha\prime) \geqslant 0$, must be fulfilled, imposing limits on the values of α. Here, $\alpha\prime$ is the angle between $\hat{r}_1$ and $\hat{n}$, called the SSS pitch angle.

However, under real conditions, the sail exhibits non-ideal optical behavior, due to the interaction of the solar electromagnetic radiation with the SSS surface, which can be reflected, absorbed or transmitted. Therefore, one can write:

$$\rho + \mathrm{\alpha} + \tau = 1, \tag{15}$$

where ρ, α and τ are the optical properties of the SSS material, spectral hemispherical reflectivity, absorptivity and transmissivity, respectively. These properties are functions of both wavelength λ and temperature $\mathscr{T}$, i.e. $\rho = \rho(\lambda, \mathscr{T}), \mathrm{\alpha} = \mathrm{\alpha}(\lambda, \mathscr{T})$ and $\tau = \tau(\lambda, \mathscr{T})$. Considering the reflective side of the sail, $\tau = 0$, therefore $\mathrm{\alpha} = 1 - \rho$. Of all incident photons, a portion will be absorbed by the sail and then re-emitted as thermal radiation, while a fraction will be reflected by specular and diffuse reflection. By taking all these effects into account, a more general formulation can be derived for a non-perfectly reflecting solar sail, given by (see also McInnes, 1999):

$$\underline{a} = \frac{1}{2}\beta \frac{1-\mu}{\|\underline{r}_1\|^2} (\hat{n} \cdot \hat{r}_1)(b_1 \hat{r}_1 + (b_2 (\hat{n} \cdot \hat{r}_1) + b_3)\hat{n}), \tag{16}$$

where the coefficients b_1, b_2, b_3depend on the sail's optical and thermo-physical properties and are defined as:

[7] we will use the comma in the subscript or superscript to indicate that the expression applies separately to each of the variables before and after the comma.

[8] we will use the subscript with a state variable to indicate a partial derivative.

[9] which is defined as absolute measure of radiated electromagnetic energy per unit time, and it is equal to $L_\odot = 3.8275 \times 10^{26}$ W.

[10] which is equal to $c = 2.9979 \times 10^8$ m/s.

$$b_1 = 1 - \rho s, \quad b_2 = 2\rho s, \quad b_3 = B_f(1-s)\rho + (1-\rho)\frac{\epsilon_f B_f - \epsilon_b B_b}{\epsilon_f + \epsilon_b}, \tag{17}$$

where s is the specular reflection coefficient, ϵ_f and $\epsilon_b$are the front and back emissivities, and B_f and $B_b$are the front and back non-Lambertian reflection coefficients, respectively. The parameters b_1, b_2, b_3 effectively describe the relative contributions of reflection, absorption, and re-emission to the total radiation pressure force.

2.3. Equilibria and the associated attitude angles

In the presence of SRP acting on an arbitrarily oriented sail, the PCR3BP is generally non-conservative. However, a conservative formulation is recovered when $\hat{n} \times \hat{r}_1 = \underline{0}$, i.e., when the sail normal is aligned with the Sun-spacecraft direction. In this case, the total potential Γ becomes

$$\Gamma = U - \frac{1}{2}\beta\frac{(1-\mu)}{\|\underline{r}_1\|}(b_1 + b_2 + b_3) \tag{18}$$

If we consider this conservative case, the number of equilibrium points remains equal to five, as in the classical CR3BP. However, their positions are slightly shifted due to the additional force introduced by SRP, which displaces the balance point toward the radiating primary.

A new class of photo-gravitational L_1-type equilibrium points can be defined, hereafter named L_1^*, by imposing $\bar{y} = 0$ and $\bar{z} = 0$, with the equilibrium located between the two main primary and CR3BP L_1. Under these assumptions, $\hat{n}\|\hat{r}_1$, meaning that these L_1^* points correspond to those of the conservative PCR3BP. This condition also implies $\bar{\alpha} = 0$, while $\bar{\delta}$ is not defined. Under these assumptions, imposing the equilibrium conditions makes the y and z differential equations in Eq. (9) identically satisfied, while the x differential equation provides the scalar equilibrium condition for the corresponding $\bar{x}$ coordinate. This condition holds for both the non-ideal optical sail model and the purely reflective case, yielding
t

$$\beta = \frac{2}{(1-\mu)(b_1+b_2+b_3)}\left(1 - d_{L_1^*}\right)^2\left(d_{L_1^*} - 1 + \mu + \frac{1-\mu}{\left(1-d_{L_1^*}\right)^2} - \frac{\mu}{d_{L_1^*}^2}\right), \tag{19}$$

with $d_{L_1^*}$ as the L_1^* distance from Earth/Moon's system CoM, defined as

$$d_{L_1^*} = -\bar{x} + 1 - \mu. \tag{20}$$

3. Optical and thermal degradation of sail materials

SSSs are ultralight reflective membranes that utilize radiation pressure from the Sun for propulsion. A summary of launched SSS missions and their respective statuses (success or failure) is provided in review (Ancona and Kezerashvili, 2025). In missions involving space-based geoengineering or deep-space exploration, placing SSSs at the $\odot - \oplus\rangle$ L_1 point provides maximum continuous solar flux, optimizing radiation pressure for propulsion without Earth's orbital shadowing or significant variation in illumination geometry. However, this position subjects the sail to degradation mechanisms that threaten structural integrity and reflectivity over time. Understanding these degradation pathways is essential for material selection and mission longevity.

3.1. Environmental conditions at L_1

Several solar and Earth observatory space mission, such as WIND, the Solar and Heliospheric Observatory (SOHO), the Advanced Composition Explorer (ACE), and the Deep Space Climate Observatory (DSCOVR), are currently operating near the $\odot - \oplus\rangle$ Lagrange point L_1, [11]. This location provides a strategic position for continuous monitoring of the solar wind, which typically reaches L_1 about one hour before interacting with the Earth's magnetosphere. At the L_1 point, a SSS is exposed to the full spectrum of solar electromagnetic radiation as well as to high-energy elementary particles such as electrons, protons, neutrinos, and ions of light nuclei emitted by the Sun. Continuous electromagnetic radiation in the range of approximately 300–2500 nm provides the propulsive pressure that enables SSS dynamics, whereas charged particles in the solar wind, such as protons, electrons, and alpha particles, contribute significantly to material degradation. In addition, the SSS materials also experience degradation due to the absorption of radiation, which leads to an increase in temperature and thermal cycling due to attitude changes. Consequently, the sail's reflectivity, emissivity, and tensile strength may deteriorate over time, and induce mass loss through thermal desorption or sputtering.

3.2. Highly reflective materials for SSS

Aluminum. Aluminum foil has long been considered as one of the most suitable materials for SSS applications due to its high reflectivity and low density.

Recent advances in material science have introduced a new generation of ultra-lightweight and radiation-resistant polymers and coatings suitable for SSS applications. Materials such as Mylar and CP1 (Colorless Polyimide version 1), a high-performance transparent polyimide film developed by NASA (Nehls, 2005), polyimides combined with reflective layers (e.g., silver or aluminum) and protective oxide caps have demonstrated promising performance in maintaining high reflectivity and infrared emissivity in the vicinity of L_1.

CP1. CP1 polyimide is commonly enhanced with vapor-deposited aluminum to improve its reflectivity and thermal control properties, particularly for space applications. This metallization process involves depositing a thin aluminum layer directly onto the CP1 film, creating a composite mate-

[11] which is located approximately at a distance $d_{L_1} = 1.5 \times 10^6$ km from Earth/Moon's system CoM.

rial that combines the mechanical and thermal stability of CP1 with the reflective properties of aluminum.

In addition to aluminum, other metals such as silver and nickel can be deposited onto polyimide films to tailor its electrical and optical characteristics. For instance, silver coatings can achieve reflectivity levels up to 98%, and subsequent electrochemical deposition of metals like palladium, platinum, or gold can further enhance stability and conductivity (Kudaikulova et al., 2008). However, while a deposit of silver, palladium, platinum, or gold enhances reflectivity, electrical and optical characteristics, this dramatically increases the areal density of such composite materials. In the standard NASA model, the reflectivity of 2.5 micrometer CP1 coated with 100 nm of aluminum is around 0.91 (Heaton and Artusio-Glimpse, 2015).

Mylar. For SSS applications, Mylar is often used in a metalized form–typically coated with vapor-deposited aluminum to enhance its reflectivity and thermal performance. This composite structure exhibits initially high reflectivity (highly reflective polyester millimeter-thick film Mylar with vapor-deposited aluminum will reflect approximately 92–97% of light (McInnes, 1999)) and low emissivity due to the aluminum layer. However, while the aluminum coating initially protects the polymer base from direct exposure, prolonged radiation can cause delamination, and mechanical microcracking, particularly under γ and UV parts of the solar electromagnetic spectrum, as well as protons and α-particles bombardment. The degradation process is governed by both the metallic surface erosion and the underlying Mylar substrate embrittlement, resulting in a compounded degradation profile with potentially faster reflectivity loss than either component in isolation if the coating fails (Edwards et al., 2004a, Kang et al., 2017). Therefore, while metalized Mylar offers high initial performance, its long-term durability is less robust than radiation–hardened alternatives such as CP1 (Heaton and Artusio-Glimpse, 2015). The LightSail-1 and LightSail-2 missions employed 5 μm aluminized Mylar as the sail membrane material, chosen for its high reflectivity and flight readiness (Heaton and Artusio-Glimpse, 2015; Johnson et al., 2016; Betts et al., 2021).

Finally, in Table 1 are reported the material, optical, and thermal properties of three SSS common configurations considered, i.e., aluminum with chromium on the rear surface, aluminized CP1 and aluminized Mylar. In particular, the values reported in Table 1 are taken from (Heaton and Artusio-Glimpse, 2015), where available. The front-side emissivity values for the Al-CP1 and Al-Mylar configurations are selected consistently with the average aluminum emissivity in the operational temperature range considered in this work. The back-side emissivities are instead adopted as conservative representative values for the exposed polymer substrates.

3.3. Radiative and thermal degradation at the ☉-⊕☽ L_1 Point

In this section, we analyze the degradation of the sail characteristics due to radiation exposure and temperature dependence of its optical parameters.

For radiation-induced degradation, we considered a macroscopic approach for the description of the interaction of the corpuscular part of solar radiation, UV, and γ part of the solar spectrum (Kezerashvili and Matloff, 2007; Kezerashvili and Matloff, 2009), and the dependence of the thickness of solar sail on temperature and on wavelength of the electromagnetic spectrum of solar radiation (Kezerashvili, 2009). As far as the temperature analysis is concerned, instead, we mainly refer to that proposed by (Kezerashvili, 2014; Ancona and Kezerashvili, 2017).

3.3.1. Radiation-induced degradation

Charged particles, UV photons, and γ radiation cause damage to solar-sail materials through atomic displacements, bond scission, and ionization. The cumulative radiation damage per unit area, D_{rad}, arising from charged particles over an exposure time t, is characterized by the incident flux spectrum and a material-dependent damage yield.

We develop a model of radiation-induced degradation based on the exponential attenuation law. The natural question arising is why we chose the exponential law for the description of degradation? The reasoning is the following:

i. The exponential law is commonly chosen to describe the degradation of materials;

ii. Many degradation radiation damage follow first-order kinetics, where the rate of degradation is proportional to the remaining intact material, which naturally leads to an exponential decay law, especially in early and mid-lifetime periods of SSS materials;

Table 1
Material, optical, and thermal properties of three SSS common configurations considered, i.e., Al-Cr, CP1, Mylar.

	a) Al-Cr	**b) Al-CP1**	**c) Al-Mylar**
Front-side material	Al	Al	Al
Back-side material	Cr	CP1	Mylar
Initial reflection coefficient ρ_0	0.88	0.91	0.95
Specular reflection factor s	0.94	0.94	0.94
Front-side emissivity ϵ_f	0.050	0.045	0.045
Back-side emissivity ϵ_b	0.55	0.50	0.45
Front-side non-Lambertian coeff. B_f	0.79	0.79	0.79
Back-side non-Lambertian coeff. B_b	0.55	0.67	0.67

iii. Radiation damages due to protons, α-particles, UV, and γ radiation are random processes. If damage occurs due to random events, and each event has a small, independent probability of causing failure or weakening, the cumulative effect over time resembles an exponential process;

iv. Finally, the exponential function is analytically convenient and easy to use in simulations, mission design, and optimization. Exponential function reflects the underlying physics of first-order processes, and allows analytical and numerical treatment in mission modeling.

Generally, it is possible to capture the essential optical behaviour of the sail by analyzing the variation of reflectivity coefficient ρ since the dominant variations in the SRP force arise from changes in it, whose variations produce the largest changes in both the normal and tangential components of the acceleration (Dachwald et al., 2005).

The degradation of reflectivity $\rho = \rho(t)$ as a function of time can be modeled as:

$$\rho = \rho_0 \; e^{-\alpha D_{rad}}. \tag{21}$$

In Eq. (21), we assume that $D_{rad} = D_{rad}(t)$ is the cumulative radiation dose induced by protons and α-particles as a function of time, α is a material-specific degradation coefficient, and ρ_0 is the initial reflectivity.

Assuming a constant solar wind and radiation flux, the dose-time relationship for all materials can be approximated as:

$$D_{rad} = \phi_0 \; t, \tag{22}$$

where $\phi_0$is the constant radiation dose rate in μC/cm^2/year and t is time in years for protons or α particles. Based on the total radiation dose rate ϕ_0 at a distance of 1 AU from solar wind protons (in this case $\phi_0 \equiv \phi_p$) and α-particles (in this case $\phi_0 \equiv \phi_\alpha$), the total radiation dose rate can be approximated in terms of electric charge per unit area.

For the solar wind proton flux in the range of 1×10^8 to 1×10^9 protons/cm^2/s, and considering the average value of 5×10^8 protons/cm^2/s, the total radiation dose rate in terms of electric charge per unit area is:

$$\phi_p \approx 2520 \, \mu\text{C}/\text{cm}^2/\text{year}. \tag{23}$$

However, in some lab simulations for modeling purposes and material degradation experiments, a more conservative $\phi_p \approx 100 - 200 \, \mu$C/cm^2/year value is sometimes used.

The solar wind at the $\odot$ – ⊕☽ L_1 point consists primarily of charged particles, predominantly protons, accompanied by a smaller but non-negligible population of alpha particles (He^{2+}). α-particles typically constitute 4–5% of the proton population, yielding an average alpha particle flux of approximately:

$$\phi_\alpha \approx (1 - 2.5) \times 10^7 \text{ particles}/\text{cm}^2/\text{s}, \tag{24}$$

assuming a typical proton flux of $\phi_p \approx 5 \times 10^8$ particles/cm^2/s. These values are based on in situ measurements from L_1-orbiting spacecraft such as *WIND* and *ACE*.

Although less numerous than protons, α-particles possess greater mass and twice the electric charge, enabling them to transfer more momentum and energy upon impact. This enhances their potential to induce sputtering, lattice displacement, and surface chemical modifications, especially in reflective and emissive materials like metalized Mylar, CP1, or bare aluminum.

The α-particle effect on optical degradation can be incorporated by adjusting the net degradation coefficient to account for both particle types:

$$a_\alpha = \kappa a_p, \tag{25}$$

with $\kappa \approx 4\eta$, where factor ≈ 4 reflects the relative increase in energy transfer from α-particle due to their higher mass and charge and $\eta = 0.045$ reflects the fact that α-particles typically constitute 4–5% of the proton population. Despite their lower flux, α-particle can disproportionately impact reflectivity, emissivity, and surface integrity due to their higher damage cross-section. Accordingly, long-duration material degradation models for SSS at L_1 must include contributions from both protons and α-particles. Degradation of SSS materials due to γ rays and UV radiation is a critical component of long-term performance modelling, especially at the $\odot$ – ⊕☽ L_1 point, where materials are continuously exposed to unfiltered solar radiation. Particularly, UV radiation leads to chain scission in Mylar and CP1 polyimides, surface embrittlement, and loss of reflectivity. The γ radiation causes ionization damage in polymers and a metallic layer, degrades molecular chains, and can change thermal and optical properties of the SSS materials.

Although spectroscopic measurements show variation of UV and γ radiations Rottman (2005, 2023), we assume constant solar UV and γ radiation fluxes, and the dose-time relationship for all materials can be approximated by a linear dependence on time given by Eq. (22) with the initial ϕ_{UV} and ϕ_γ fluxes, respectively. In this case, like with particle-induced degradation, the exponential decay model in Eq. (21) can be used for reflectivity degradation with material-specific dose functions:

$$D_{UV} = \int_0^t \phi_{UV} \; dt' = \phi_{UV} \; t, \quad D_\gamma = \int_0^t \phi_\gamma \; dt' = \phi_\gamma \; t, \tag{26}$$

where ϕ_{UV} and ϕ_γ are the spectral UV and γ-radiation fluxes at the surface, in W/cm^2, respectively. The assumption of the constant radiation fluxes in Eqs. (26) leads to the linear dependence of $D_{UV} = D_{UV}(t)$ and $D_\gamma = D_\gamma(t)$ on time. The corresponding degradation coefficients a_{UV} and a_γ in cm^2/J in Eq. (21) are material-specific.

Based on the inverse square law the energy flux Φ (also said solar irradiance) depends on the norm of the Sun-SSS position vector $\underline{r}_1$ as:

$$\Phi = \Phi_0 \frac{\cos(\alpha')}{\|\underline{r}_1\|^2}, \quad \Phi_0 = \frac{L_\odot}{4\pi D_\odot^2}, \tag{27}$$

where Φ_0[12] is the Solar irradiance at $D_\odot$, which is the dimensional Sun distance from Earth/Moon's system CoM and equal to L, defined through the solar luminosity $L_\odot$ and $\alpha\prime$ is the sail pitch angle between the normal of the SSS $\hat{n}$ and $\underline{r}_1$.

The cumulative average UV flux $\phi_{\rm UV}$, which is commonly subdivided into UV-A, UV-B, and UV-C, can be estimated from the total solar irradiance at 1 AU. The most harmful component for material degradation is UV-C radiation (100–280 nm) (NASA, 2024), which contributes roughly 1–1.5 W/m^2, or approximately 0.1% of the total solar electromagnetic radiation. Therefore, the UVC energy per unit area received over a year is estimated as:

$$\phi_{UV} \approx 4.3 \times 10^3\ \mathrm{J/cm^2/year}. \tag{28}$$

γ rays are high-energy photons (with energies above $\sim$100 keV and wavelengths $<$ 0.01 nm) emitted primarily in the solar core due to proton-proton chain reactions. Though largely absorbed internally, a small flux can escape, especially during solar flares. During quiet solar conditions, the gamma-ray contribution is less than 0.000001% (Rottman, 2005) of total solar radiation, but can briefly increase by an order of magnitude during strong solar flares.

Thus, the annual γ energy deposition per unit area is:

$$\phi_\gamma \approx 4.3 \times 10^{-3}\ \mathrm{J/cm^2/year}. \tag{29}$$

Assuming constant fluxes for simplicity, we can write for practical simulation the following generalized model for reflectivity degradation via environmental conditions near L_1 point:

$$\rho = \rho_0 e^{-\Lambda t}, \tag{30}$$

where

$$\Lambda = a_p\phi_p + a_\alpha\phi_\alpha + a_{UV}\phi_{UV} + a_\gamma\phi_\gamma \tag{31}$$

is an effective total degradation rate combining all mechanisms of degradation.

Considering Eqs. (30) and (31) the degradation of reflectivity for each material, can be modeled using the following exponential decay expressions:

$$\rho_i = \rho_{0_i} e^{-\Lambda_i t}, \tag{32}$$

where ρ_{0_i} and Λ_i denote the initial reflectivity and degradation rate of material i, with $i =$Al, CP1, Mylar. These equations provide a direct means to simulate reflectivity degradation over mission time, given a known or assumed radiation environment.

We perform the modeling based on a material-specific approach under integrated solar wind, UV, and γ radiation conditions. Table 2 lists estimated degradation coefficients for Aluminum, Mylar and CP1. They were estimated based on experimental and modeling data available in the literature for materials of similar composition and radiation exposure conditions.

The values for protons and α-particles were guided primarily by the NASA *Radiation Effects Design Handbook* (Hanks and Hamman, 1971), which provides order-of-magnitude degradation data for insulating and metallic materials under charged-particle irradiation. Estimates for UV degradation were inferred from polymer aging studies under photo-oxidative environments (Lu et al., 2018; Maraveas et al., 2024), while the coefficients for γ-ray exposure were adapted from recent investigations of polyimide film degradation under ionizing radiation (Shen et al., 2020). Given that published data are often reported for specific experimental conditions and dose units, the coefficients in Table 2 should be regarded as approximate, representing the typical order of magnitude for reflectivity loss in Aluminum, Mylar, and CP1 films under prolonged exposure to space radiation. Future experimental work will be required to refine these estimates for solar-sail applications.

It is important to note that coefficients in Table 2 are approximately estimated from heterogeneous sources with differing irradiation energies, fluxes, and environmental conditions. Therefore, they should be regarded as approximate, order-of-magnitude parameters intended for parametric modeling rather than precise prediction. The results presented here are thus indicative of general trends in reflectivity degradation under prolonged space radiation exposure. Dedicated experiments under mission-relevant conditions will be required to refine these coefficients for accurate solar sail performance predictions. One important experimental effort in this direction involves the study of the progression of reflectance degradation caused by hydrogen recombination processes and hydrogen blistering (Sznajder et al., 2015; Sznajder et al., 2018; Sznajder et al., 2020; Klein et al., 2026).

In calculating the reflectivity degradation of the sail material due to proton and α-particle impact, we use the following assumptions. First, we adopt a conservative value of $\phi_0 = 200\,\mu\mathrm{C/cm^2/year}$ (ECSS, 2019), which is typically used in laboratory simulations to model the average total radiation dose rate, and we also consider the case in which this dose rate increases by a factor of 10 as in Eq. (23). In addition, we examine the most extreme case and further increase of the last value by another factor of 10, giving $\phi_0 = 25000\,\mu\mathrm{C/cm^2/year}$, which may occur during periods of high solar activity. However, such a high flux is realistic only for short time intervals.

Results of the modeled reflectivity degradation over a mission lifetime of several years in solar-radiation-rich environments are presented in Fig. 2. It compares the degradation of the reflectivity for aluminum, CP1, and Mylar based on the exponential decay model. CP1, a radiation–hardened polyimide used in multilayer sail structures, exhibits much slower degradation. CP1 demonstrates superior long-term stability, while Mylar

[12] which is equal to $\Phi_0 = 1346\mathrm{W/m^2}$

Table 2
Initial reflectivity and approximate degradation coefficients due to protons and α-particles impact as well as UV and γ rays exposure for selected sail materials.

Material	ρ_0	α_p ($cm^2/\mu C$)	α_α ($cm^2/\mu C$)	α_{UV} (cm^2/J)	α_γ (cm^2/J)	Λ (1/year)
Aluminum	0.88	1.5×10^{-5}	1.7×10^{-6}	$\sim 1.5 \times 10^{-6}$	$\sim 2.0 \times 10^{-7}$	3.42×10^{-3}
CP1	0.91	1.0×10^{-6}	1.1×10^{-7}	$\sim 1.5 \times 10^{-7}$	$\sim 1.0 \times 10^{-7}$	4.82×10^{-2}
Mylar	0.95	5.0×10^{-6}	5.6×10^{-7}	$\sim 1.0 \times 10^{-6}$	$\sim 1.0 \times 10^{-6}$	1.82×10^{-2}

retains high initial reflectivity but degrades faster than CP1. Mylar initially has high reflectivity ($\rho_0 \approx 0.95$) but suffers from UV embrittlement and radiation-induced microcracking over time. Results of calculations show that aluminum reflectivity degrades under UV, γ, and charged particle exposure. Aluminum exhibits moderate degradation compared to Mylar, but it remains a reliable choice when combined with protective coatings or used in laminated structures.

The radiation-induced degradation model developed in this study is incorporated into the equations of motion to capture the time evolution of the sail's optical properties. In particular, in order to provide a basis of comparison with existing models, in particular the Dachwald et al. (Dachwald et al., 2006), we propose now a general formulation that extends that model by introducing multiple degradation sources and material-specific degradation coefficients, as detailed before in Section 3. Within this framework, the time-dependent reflectivity degradation depends directly on Λ_i, which represents the effective total degradation rate (see Eq. (31)). This parameter combines the contributions from charged particle fluxes, UV radiation, and γ radiation, and is specific to each material type (e.g., Aluminum, CP1, Mylar). In the parametric formulation of Dachwald et al. (Dachwald et al., 2006), the time-dependent reflectivity is given by

$$\rho = \rho_0 \frac{1 + d\, e^{-\lambda\Sigma}}{1 + d}, \tag{33}$$

where λ is a degradation constant, d is a degradation factor, and $\Sigma = \Sigma(t)$ represents the non-dimensional deviation, over time, of the solar radiation dose received by the sail surface with respect to a reference value (the one at 1 AU), which includes the correction due to a Sun distance different from 1 AU and for different attitude $\cos(\alpha\prime)$. By considering a giving

$$\Sigma = \frac{1}{T} \int_{t_0}^{t} \frac{\cos(\alpha\prime)}{\|\underline{r}_1\|^2} dt\prime \tag{34}$$

in our formulation, we retain the degradation factor d, which determines the asymptotic reflectivity through $\rho_\infty = \rho_0/(1 + d)$, but replace the term λ with $\Lambda T$for a more comprehensive rate decay formulation. Indeed, in the original formulation by (Dachwald et al., 2006), the degradation rate λ is related to the half-life solar radiation dose. This assumption provides a convenient way to define the degradation rate, but it does not explicitly account for the physical sources contributing to the degradation process.

In the present work, the coefficient λ (or equivalently its associated ratio) is instead given a more explicit physical interpretation by considering multiple degradation mechanisms and radiation sources. This leads to an extended formulation in which the degradation parameter represents the combined effect of different physical processes acting on the sail material.

This yields a unified expression:

$$\rho = \rho_0 \frac{1 + d\, e^{-\Lambda T\Sigma}}{1 + d} = \rho_0 \frac{1 + d\, e^{-\Lambda \int_{t_0}^{t} \frac{\cos(\alpha\prime)}{\|\underline{r}_1\|^2} dt\prime}}{1 + d}. \tag{35}$$

With respect to Eq. (32), Eq. (35) generalizes the degradation influence by considering also a possible steady state with the degradation factor d and the correction due to a change in position or attitude for the dose coefficients, used in calculating Λ, with the factor Σ.

Since other optical coefficients also play a major role in the sail dynamics, a similar degradation law is applied also

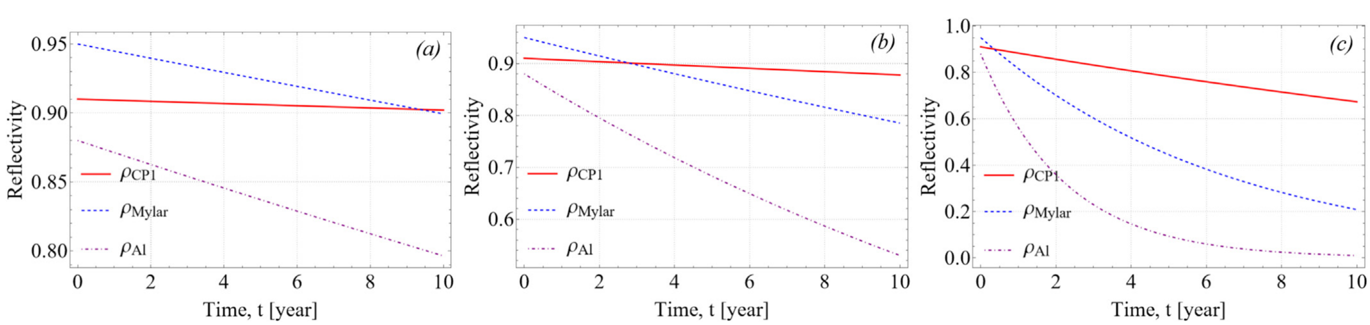

Fig. 2. Modelled reflectivity degradation of Aluminum, CP1, and Mylar over mission duration under integrated solar wind conditions and constant radiation dose: (a) conservative value 200 $\mu C/cm^2$/year used in material degradation experiments; (b) the average value of 2500 $\mu C/cm^2$/year; and (c), average flux increased by a factor of 10, 25000 $\mu C/cm^2$/year due to higher solar activity. The last value for the flux is realistic only for short time durations.

for the specular reflectivity and the front-side emissivity as in (Dachwald et al., 2006), giving

$$s = s_0 \frac{1 + d\,e^{-\Lambda \int_{t_0}^{t} \frac{\cos(\alpha\prime)}{\|\underline{r}_1\|^2} dt\prime}}{1+d}, \quad \epsilon_f = \epsilon_{f_0}\left(1 + d\left(1 - e^{-\Lambda \int_{t_0}^{t} \frac{\cos(\alpha\prime)}{\|\underline{r}_1\|^2} dt\prime}\right)\right), \tag{36}$$

The remaining parameters, namely the back-side emissivity, and the non-Lambertian coefficients, are considered constant. Moreover, we consider that the optical coefficients do not depend on $\alpha\prime$ as well as no self-healing effects occur in the SSS. Instead, the dependence on temperature is now discussed.

3.3.2. Solar-Sail Temperature at the L_1 Point

While the previous subsection focuses on radiation-induced degradation, temperature is another key factor affecting the long-term reflectivity and emissivity of SSS materials.

Recent studies show that reflectivity and emissivity also depend on the temperature (Kezerashvili, 2014). Although reflectivity's dependence on temperature can be neglected, the same does not apply for emissivity, which is directly proportional to the temperature, as suggested by Parker and Abbott in (Parker and Abbott, 1965).

The temperature of the SSS surface depends on the heliocentric distance (Polyakhova, 1986; McInnes, 1999; Kezerashvili, 2014; Ancona and Kezerashvili, 2017). As shown in (Kezerashvili, 2014; Ancona and Kezerashvili, 2017; Ancona and Kezerashvili, 2019), for electrically conductive materials the dependence of temperature on heliocentric distance has an exponential index proportional to $-2/5$, while a more conservative approach leads to a dependence of $-1/2$ (Polyakhova, 1986; McInnes, 1999). The sail temperature can be estimated using the law of conservation of energy, accounting for the temperature-dependent optical properties of the sail material, such as reflectivity, absorptivity, and emissivity (Kezerashvili, 2014). In the analysis below, we adopt the more conservative approach, assuming that the reflectivity and emissivity of the material are constant and do not depend on temperature.

Due to the effect of temperature on the radiative and optical properties, the corresponding absorbed energy flux Φ_a will be:

$$\Phi_a = (1 - \rho - \tau)\Phi, \tag{37}$$

where the dependence on wavelength has been removed by computing the spectral average, so considering the total hemispherical optical coefficients.

Once that energy has been absorbed, it can also be emitted from the surface, as a secondary process. From the Stefan–Boltzmann's law, the rate of energy emitted from a surface at a certain temperature is proportional to the fourth power of the temperature $\mathscr{T}$. As a sail is usually composed by various films of different materials, in general its front and back sides will have different emissivity, ϵ_F and ϵ_B, respectively. Hence, the emitted energy flux Φ_e, from front and back surfaces is:

$$\Phi_e = (\epsilon_F + \epsilon_B)\sigma_{SB}\mathscr{T}^4, \tag{38}$$

where σ_{SB}[13] is the Stefan–Boltzmann constant. From the law of conservation of energy, the SSS will be in thermal equilibrium if the total absorbed energy equals the total emitted energy. By applying the equality $\Phi_e = \Phi_a$, the so known Kirchhoff's law, and considering that from Eq. (27) the solar energy flux has an inverse square variation with the heliocentric distance, one can find the dependence of the sail temperature on the heliocentric distance as

$$\mathscr{T} = \left(\frac{(1-\rho-\tau)\,\Phi_0 \cos(\alpha\prime)}{(\epsilon_F + \epsilon_B)\,\sigma_{SB}}\right)^{1/4} \sqrt{\frac{1}{\|\underline{r}_1\|}}. \tag{39}$$

Table 3
Approximate emissivity of materials versus temperature.

Material	300 K	600 K	800 K	1000 K	1200 K	1400 K
Aluminum	0.04	0.05	0.07	0.10	0.15	0.20
CP1	0.10	0.12	0.13	0.14	0.15	0.16
Mylar	0.03	0.035	0.04	0.05	0.06	0.07

The analysis of Eq. (39) shows that the temperature depends on the sail material's reflectivity ρ and emissivity ϵ. In Table 3, the emissivities of the sail materials are presented at different temperatures based on the cumulative data from Refs. (Kleiman and Tennyson, 1999; NASA, 1972; Touloukian and DeWitt, 1972; Modest, 2013; DuPont, 2013; ESA, 2015), and dependence of the emissivity on temperature are illustrated in Fig. 3. Analysis of the data presented in Table 3 demonstrates that the emissivity of polished aluminum starts around 0.04 and increases up to approximately 0.2 at 1400 K. Recently engineered material, such as CP1, exhibits thermal properties that result in equilibrium temperatures comparable to those at the ⊙ – ⊕☽ L_1 point (Loke et al., 2022). The emissivity of CP1 is moderately low, generally in the range of 0.1–0.16, within the temperature range of 300 – 1400 K. The emissivity of Mylar is even lower, ranging from 0.03 to 0.07, depending on temperature and surface coating.

The reflectivity of the Aluminum decreases slightly with temperature, mainly in the infrared range by 1–3% in the temperature window 300 K to 600 K. Reflectivities of Mylar and CP1 come from the aluminum coating. Therefore, their reflectivities are of the same order as for the Aluminum.

The temperature dependence due to radiation-induced degradation over the mission duration can be taken into account by substituting Eqs. (32) into Eq. (39). Consideration of radiation-induced degradation leads to an increase in the sail material temperature.

[13] which is equal to $\sigma_{SB} = 5.67 \times 10^{-8}$ Wm^{-2}K^{-4}

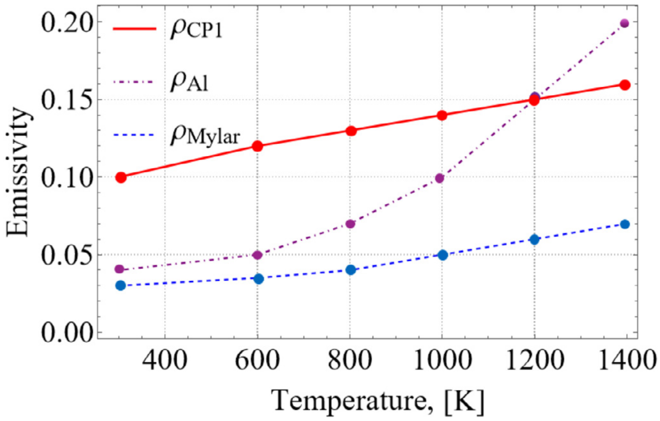

Fig. 3. Emissivity versus temperature for Aluminum, Mylar, and CP1.

4. Case study - planetary sunshade system

The Planetary Sunshade represents a space-based geoengineering concept aimed at mitigating climate change by reducing the solar radiance reaching Earth. This concept and its phased development pathway are described in detail in a companion roadmap study (Matonti et al., 2026). Positioned between Sun and Earth, the system would cast a partial shadow on Earth, contributing to global temperature stabilization (see Fig. 4). Beyond technical feasibility, the Planetary Sunshade aligns with global climate action frameworks (e.g., UN SDG 13 (United Nations, 2026)). It offers a reversible, non-terrestrial intervention that complements emission reduction strategies. However, governance, ethical considerations, and international collaboration remain critical to its implementation (Chesley et al., 2023; Romano et al., 2023).

Generally, the main strategy consists of a swarm of SSS capable of active control, which can be either totally or partially assembled to build one or more occulting disks (Roger, 2006; McInnes, 2010). Given that the required solar radiance reduction may involve millions of units, effective swarm formation flying and control become critical challenges. The swarm astrodynamics, including the study of suitable families of L_1^* Halo orbits, has been extensively investigated in (Matonti et al., 2023b; Matonti and Romano, 2024), along with various orbital transfer strategies (Fuglesang and de Herreros Miciano, 2021; Matonti et al., 2023a). The optimal configuration to avoid unintended climate consequences has also been investigated in (Sánchez and McInnes, 2015; Oggionni et al., 2022). Finally, alternative architectures exploring space resources have been proposed (Jehle et al., 2020; Baum et al., 2022).

The Planetary Sunshade concept considered here consists of a swarm of SSS operating in non-Keplerian orbits near the minimum-mass L_1^* point. Each unit uses SRP for station-keeping, reducing or obviating the need for propellant, a critical constraint for long-duration missions. The primary objective is to achieve a controlled reduction in solar flux (typically 0.5–2%) to counteract greenhouse gas-induced warming, while maintaining reversibility and operational flexibility (Govindasamy and Caldeira, 2000).

The Planetary Sunshade architecture must incorporate strategies to mitigate the effects of material degradation and ensure long-term operational reliability. Key considerations for sustained mission performance include integrating degradation models directly into sail guidance

Fig. 4. Conceptual visualization of a Planetary Sunshade.

algorithms to maintain control authority over extended mission durations. Furthermore, it is essential to optimize sail positioning strategies to maximize the effective shading area while minimizing the number of deployed units. Design efforts must also consider sails sizing margins or reserve modules to compensate for performance losses due to optical and thermal degradation. Operationally, this requires implementing autonomous formation control and reconfiguration algorithms to preserve swarm geometry under dynamic perturbations, and establishing maintenance protocols, such as periodic repositioning or replacement of degraded units, to sustain system-level performance. These measures collectively enhance system resilience, maintain shading effectiveness, and reduce the risk of mission failure under prolonged exposure to the harsh space environment.

A series of precursor missions should be designed to test the long term performance around L_1^* (Coco et al., 2025; Matonti et al., 2026), and the adoption of Extended Reality immersive environments is programmed for operational planning and maintenance simulation (Matonti et al., 2025).

Table 4 reports the main orbital and system requirements of the single SSS module of a possible precursor mission. Starting from this, we define a use case for the subsequent orbital degradation simulations section, where the ideal lightness number is intended for a perfectly reflecting surface. In case of a non-ideal optical behavior, the lightness number β is given by

$$\beta = \frac{2\beta\prime}{b_1 + b_2 + b_3}. \tag{40}$$

Moreover, at this L_1^*, we may assume that the reflectivity of the materials remains constant in the temperature range $300 - 600\,\mathrm{K}$. To prove this, we now determine the corresponding equilibrium temperature of the SSS material at this location. The equilibrium temperature in a worst-case scenario can be estimated by considering the emissivity at 600 K. Substituting emissivities values from Table 3 at 600 K in Eq. (39), we obtain

$$\mathscr{T}_i = \mathscr{T}_{0_i}\,(\cos(\alpha\prime))^{1/4}, \tag{41}$$

where i =Al, CP1, Mylar and $\mathscr{T}_{0_i}$ are the corresponding equilibrium temperatures for $\alpha\prime = 0$, and which are equal to $\mathscr{T}_{\mathrm{CP1}} = 338\,\mathrm{K}, \mathscr{T}_{\mathrm{Mylar}} = 347\,\mathrm{K}$, and $\mathscr{T}_{\mathrm{Al}} = 414\,\mathrm{K}$. It should be emphasized that these temperatures are calculated under the assumption that radiation-induced degradation of the sail materials is neglected. Fig. 5 shows the evolution of temperature over the mission duration of 10 years due to degradation caused by solar wind, UV, and γ radiation for Aluminum, CP1, and Mylar.

Table 4
Mission and geometric parameters of the sunshade module.

Operational environment	L_1^* region
Distance from Earth	2.367×10^6 km
Dynamic model	$\odot$– $\oplus$☽ PCR3BP
Sail shape	Square
Sail area A	400 m^2
Sail mass M	16 kg
Areal mass density σ	40 g/m^2
Ideal lightness number $\beta\prime$	0.0349

In the present study, the sail is assumed to operate in the vicinity of the nominal L_1^* equilibrium configuration. Within this region, the heliocentric distance varies only over a limited range during the operational interval considered; consequently, the corresponding sail temperature remains confined to a narrow interval. Furthermore, the temperature analysis indicates that, for the materials considered here, the sail temperature remains within a range for which temperature-induced variations of the reflectivity can be neglected to first order. Therefore, the coupling between temperature evolution and orbital dynamics is neglected in the present simulations.

Following the study in Rozhkov et al. (2021), which investigated sail reflectivity as a function of material properties, sail design, temperature, multilayer thickness, and the degradation factor d, the latter was varied within the range $d = 0.1 - 0.25$ with reasonable accuracy. Assuming an average value of $d = 0.15$, we illustrate the temperature evolution in Fig. 5, which shows the variation of sail temperature over a 10-year mission duration. The model accounts for degradation due to solar wind, UV, and γ-radiation for Aluminum, Mylar, and CP1. The results presented in Fig. 5 indicate that, over the 10-year mission, the temperature of the CP1 sail increases by only about 10 K, whereas the Aluminum and Mylar sails exhibit larger increases of approximately 40 K and 35 K, respectively. Consequently, the sail material temperatures are slightly higher than those obtained from Eq. (41), where radiation-induced degradation was not taken into account.

Overall, these findings support our assumption that the temperature dependence of reflectivity and emissivity can be neglected, since the subsequent simulations consider only radiation-induced degradation effects.

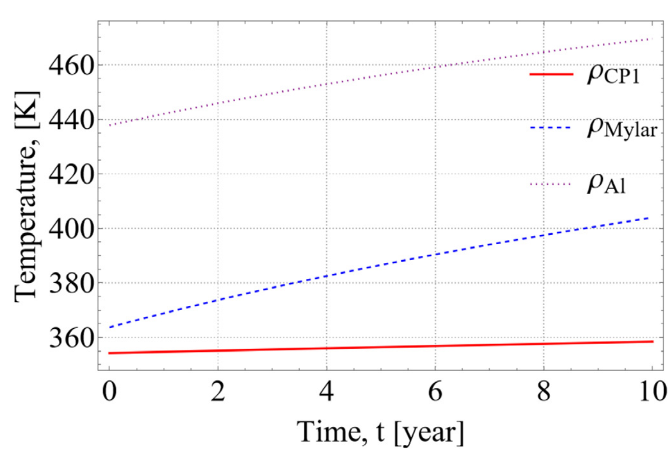

Fig. 5. Temperature increase due to degradation by solar wind, UV, and γ radiation of aluminum, CP1, and Mylar over the mission duration of 10 years.

Notice that for large-area solar sails such as Sunshade-type systems, structural effects - including deformation and wrinkling - become increasingly significant and may influence optical properties and propulsion performance. For large-scale solar sails required for mission profiles like sunshades or displaced solar orbits, the structural integrity and long-term performance are sensitive to membrane wrinkling. Unlike smaller demonstrators such as IKAROS, large sails exhibit complex wrinkling patterns that can significantly alter the effective SRP. Recent studies have demonstrated the utility of the point cloud method for analyzing large-scale deformations (Huang et al., 2021) and provided comprehensive wrinkling analyses for solar-photon sails by Vulpetti et al. (2021). These effects are particularly critical when coupled with the thermally induced structural softening discussed in this work, as they collectively determine the precision of the attitude-orbit control system. In Ref. Zou et al. (2022), authors developed a nonlinear finite-element-based method combined with experimental validation to analyze and accurately measure wrinkling behavior in solar sail membrane structures under applied loads. A fully coupled treatment of membrane wrinkling effects is beyond the scope of the present work.

5. Results

Starting from the positioning and geometric requirements of the Planetary Sunshade ⊛ reported in Table 4, we investigate the long-term effect of material degradation for the three candidate material configurations with optical and thermal properties listed in Table 1.

In this section we focus on the relative dynamical evolution of the sunshade around the L_1^* equilibrium point, comparing the three materials and introducing the parametric degradation factor d proposed in (Dachwald et al., 2006). In order to isolate the dominant contribution of the optical degradation, only the time variation of the total reflectivity ρ, specular reflectivity s and front-side emissivity ϵ_f is considered, while all other optical and thermal parameters are kept constant as per Table 1. In the limit $d \to \infty$ the Dachwald model tends to the exponential–decay expression introduced in Eq. (32), so that the two formulations become consistent in the asymptotic regime.

The degradation factor d is sampled over more than four orders of magnitude using a logarithmic distribution, in order to capture both the strong variability associated with low values of d and the asymptotic behavior for large d. Specifically, we consider

$$d_i = d_0 2^i, \quad \text{with} \quad i = 1, .., 17 \quad \text{giving} \quad d_i \in (0.01, 0.02, 0.04, \ldots, 10485.76), \tag{42}$$

so that consecutive values differ by a factor of two. For each material and each value of d, the equations of motion in the PCR3BP are propagated starting from the L_1^* with the equilibrium attitude ($\alpha = 0$).

The equations of motion were numerically propagated in MATLAB using a high-order adaptive Runge–Kutta integrator. In particular, a variable-step Runge–Kutta method of order 8–9 was adopted in order to ensure both numerical accuracy and computational efficiency. The relative and absolute tolerances of the integrator were set to 10^{-13} and 10^{-13}, respectively. The integration was performed in nondimensional units consistent with the adopted dynamical framework.

To quantify the deviation from the nominal configuration, we introduce two non-dimensional indicators: (i) the relative position vector error norm, and (ii) the relative velocity vector error norm, both with respect to L_1^*, defined as

$$e_r = \log_{10}\left(\|\underline{r} - \underline{r}_{L_1^*}\|\right), \quad e_v = \log_{10}(\|\dot{\underline{r}}\|), \tag{43}$$

then we define two more non-dimensional indicators: (i) the relative position vector difference norm and (ii) the relative velocity vector difference norm, both with respect to (Dachwald et al., 2006) propagation (with $\lambda = \ln\left(\sqrt{2}\right) =\sim 0.347$ as per (Dachwald et al., 2006) and two propagations with Λ incremented and decremented by 50%, defined as

$$\Delta e_r^k = \log_{10}\left(\|\underline{r} - \underline{r}^k\|\right),$$
$$\Delta e_v^k = \log_{10}\left(\|\dot{\underline{r}} - \dot{\underline{r}}^k\|\right), \qquad k = d, +, - \tag{44}$$

where k stands for (Dachwald et al., 2006) ”d”, incremented Λ by 50% ”+” and decremented Λ by 50% ”-”.

For completeness, Fig. 6 shows a zoom of the resulting trajectories in the S-CCS, centered at L_1^*, while Figs. 7–9 reports the time evolution of the total reflectivity ρ, the specular reflectivity s, and the front-side emissivity ϵ_f.

The time evolution of the position and velocity errors, e_r and e_v, is shown in Figs. 10 and 11 as a function of the mission time t, expressed in days, and of the degradation factor d. The comparison with the classical degradation model of Dachwald et al. (2006), together with the cases obtained by increasing and decreasing Λ by 50%, is reported in Figs. 12–17 for the three considered materials.

A quantitative summary of the trends observed in the contour plots is given in Tables 5–10, where the values of e_r and e_v are reported for the representative subset $d \in [0.01, 0.1, 1, 10, 100, 1000, 10000]$ and $t \in [1, 10, 100]$ days, for all three materials. These cases illustrate how the combined effect of optical degradation and intrinsic dynamical instability manifests over increasingly long time horizons. Moreover, the trajectories were propagated for approximately 100 days in order to investigate the early escape dynamics from the photo-gravitational L_1^* equilibrium point. As discussed in Section 3.3.2, the sail temperature depends primarily on the heliocentric distance. Over the considered propagation interval, the spacecraft remains within a relatively small region around the nominal operating point, resulting in only

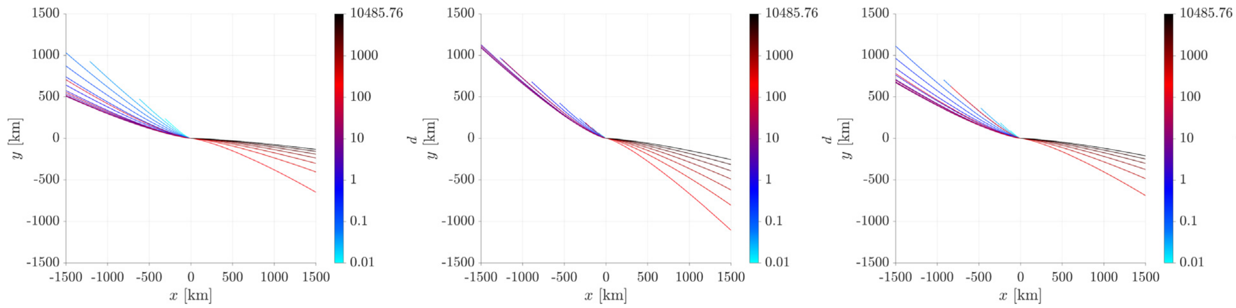

(a) Aluminum (b) CP1 (c) Mylar

Fig. 6. Trajectory with respect to L_1^*.

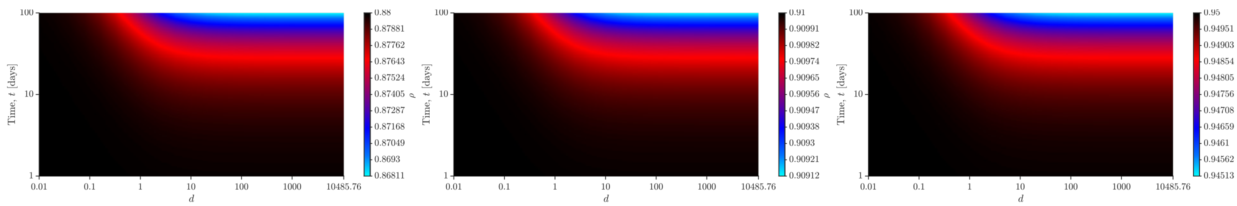

(a) Aluminum (b) CP1 (c) Mylar

Fig. 7. Total reflectivity ρ over time t and for different degradation factor d, for Aluminum *(left)*, CP1 *(center)*, Mylar *(right)*.

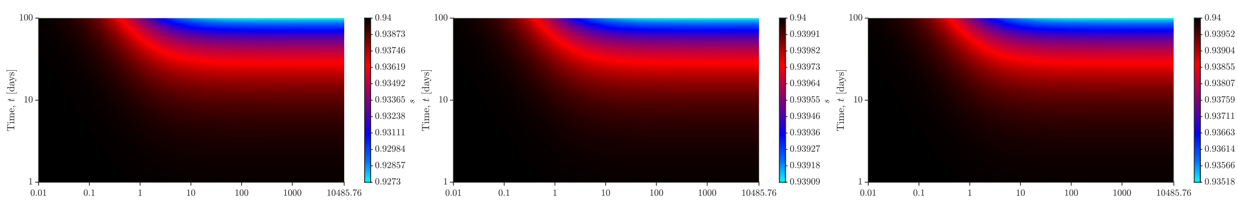

(a) Aluminum (b) CP1 (c) Mylar

Fig. 8. Specular Reflectivity s over time t and for different degradation factor d, for Aluminum *(left)*, CP1 *(center)*, Mylar *(right)*.

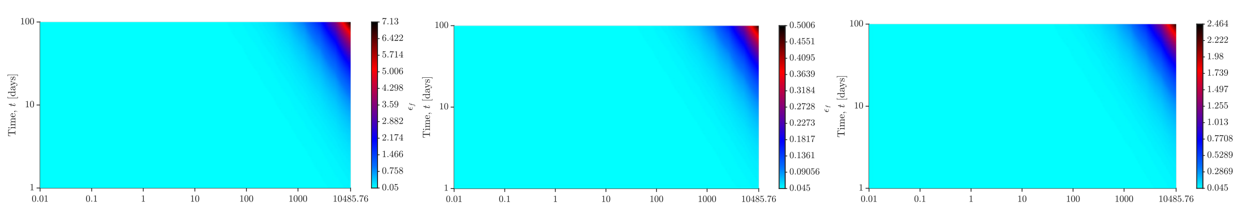

(a) Aluminum (b) CP1 (c) Mylar

Fig. 9. Front-side emissivity ϵ_f over time t and for different degradation factor d, for Aluminum *(left)*, CP1 *(center)*, Mylar *(right)*.

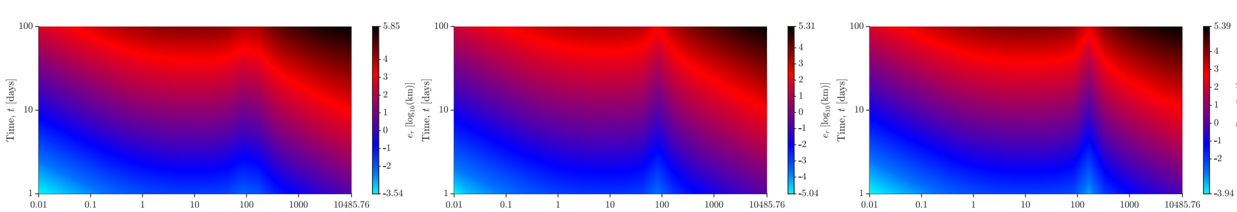

(a) Aluminum (b) CP1 (c) Mylar

Fig. 10. L_1^* relative position vector error e_r norm over time t and for different degradation factor d, for Aluminum *(left)*, CP1 *(center)*, Mylar *(right)*.

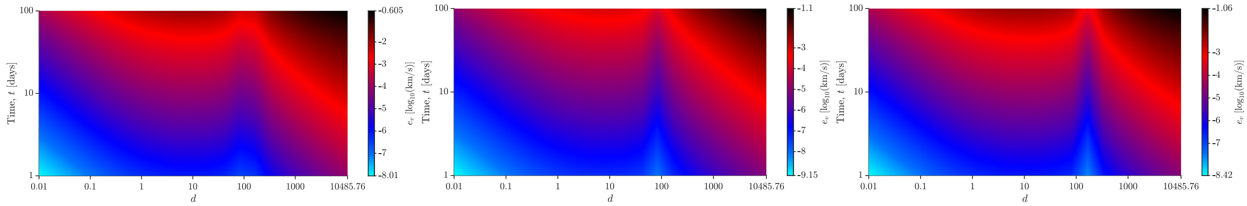

(a) Aluminum (b) CP1 (c) Mylar

Fig. 11. L_1^* relative velocity vector error e_v norm over time t and for different degradation factor d, for Aluminum *(left)*, CP1 *(center)*, Mylar *(right)*.

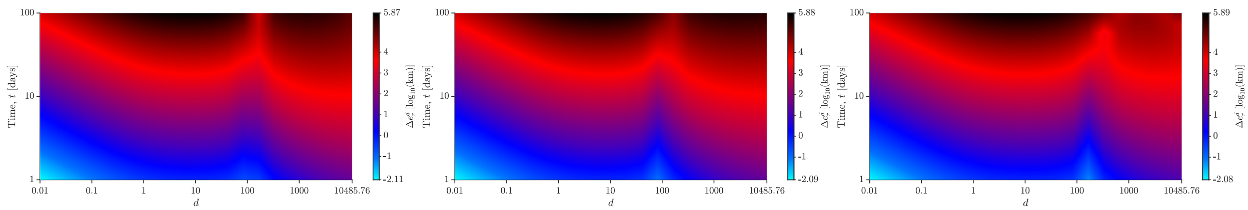

(a) Aluminum (b) CP1 (c) Mylar

(Dachwald et al., 2006)

Fig. 12. L_1^* relative position vector difference Δe_r^d norm with respect to (Dachwald et al., 2006) model over time t and for different degradation factor d, for Aluminum *(left)*, CP1 *(center)*, Mylar *(right)*.

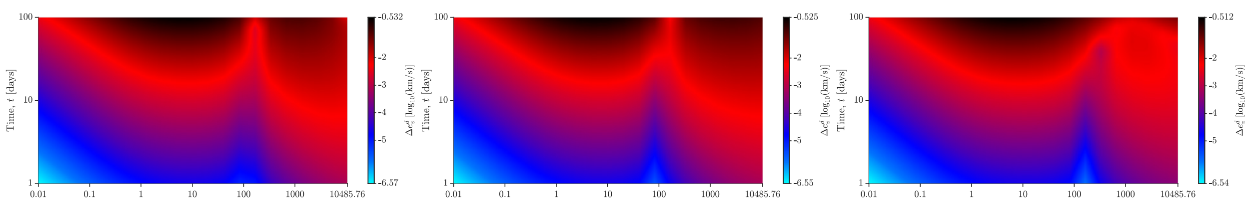

(a) Aluminum (b) CP1 (c) Mylar

Fig. 13. L_1^* relative velocity vector difference Δe_v^d norm with respect to (Dachwald et al., 2006) model, over time t and for different degradation factor d, for Aluminum *(left)*, CP1 *(center)*, Mylar *(right)*.

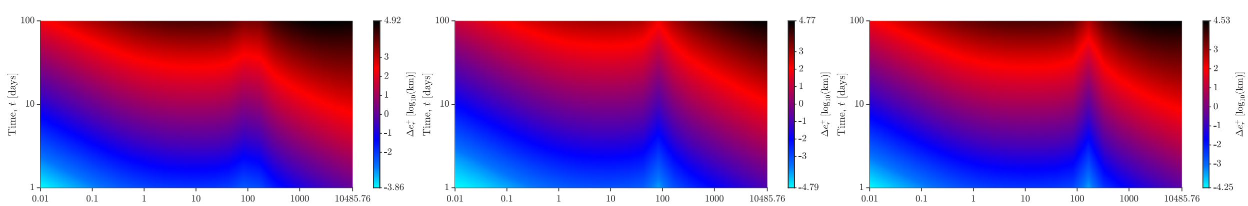

(a) Aluminum (b) CP1 (c) Mylar

Fig. 14. L_1^* relative position vector difference Δe_r^+ norm with respect to simulation with Λ incremented by 50% over time t and for different degradation factor d, for Aluminum *(left)*, CP1 *(center)*, Mylar *(right)*.

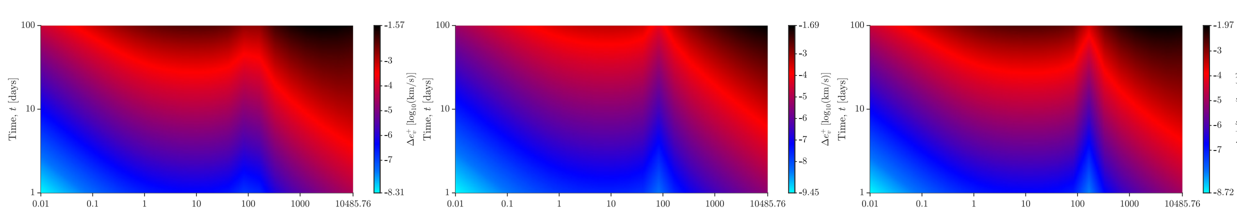

(a) Aluminum (b) CP1 (c) Mylar

Fig. 15. L_1^* relative velocity vector difference Δe_v^+ norm with respect to simulation with Λ incremented by 50%, over time t and for different degradation factor d, for Aluminum *(left)*, CP1 *(center)*, Mylar *(right)*.

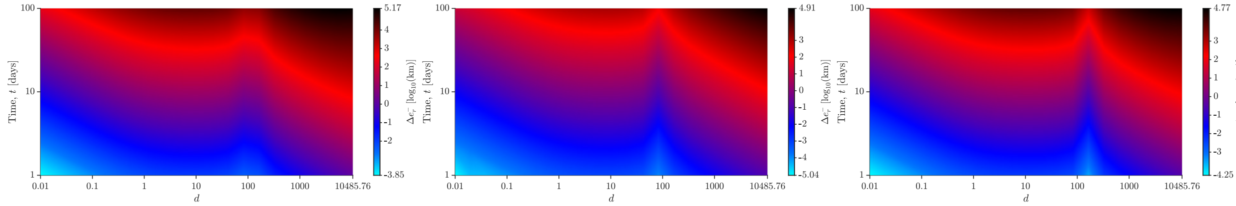

(a) Aluminum (b) CP1 (c) Mylar

Fig. 16. L_1^* relative position vector difference Δe_r^- norm with respect to simulation with Λ decremented by 50% over time t and for different degradation factor d, for Aluminum *(left)*, CP1 *(center)*, Mylar *(right)*.

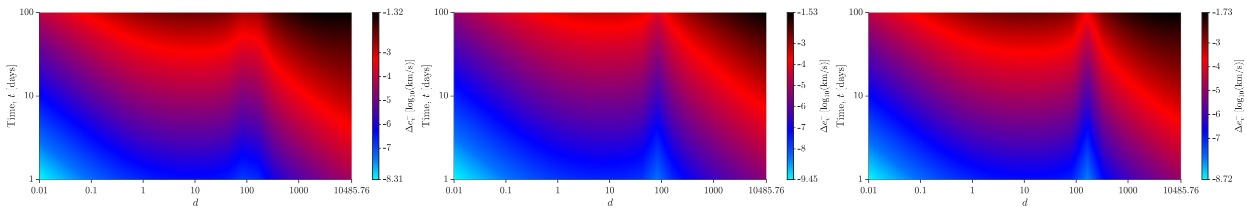

(a) Aluminum (b) CP1 (c) Mylar

Fig. 17. L_1^* relative velocity vector difference Δe_v^- norm with respect to simulation with Λ decremented by 50%, over time t and for different degradation factor d, for Aluminum *(left)*, CP1 *(center)*, Mylar *(right)*.

Table 5
L_1^* relative position vector error e_r norm [km] over time t and for different degradation factor d, for Aluminum.

t [days] ↓ / d→	0.01	0.1	1	10	100	1000	10000
1	9.21×10^{-6}	1.86×10^{-4}	9.93×10^{-4}	1.66×10^{-3}	5.29×10^{-4}	2.02×10^{-2}	2.19×10^{-1}
10	2.04×10^{-2}	1.85×10^{-1}	9.92×10^{-1}	1.67	5.28×10^{-1}	2.01×10^{1}	2.07×10^{2}
100	2.87×10^{1}	2.60×10^{2}	1.39×10^{3}	2.34×10^{3}	7.36×10^{2}	2.67×10^{4}	1.99×10^{5}

Table 6
L_1^* relative position vector error e_r norm [km] over time t and for different degradation factor d, for CP1.

t [days] ↓ / d→	0.01	0.1	1	10	100	1000	10000
1	2.87×10^{-4}	2.55×10^{-3}	1.36×10^{-2}	2.34×10^{-2}	8.90×10^{-3}	2.15×10^{-1}	2.29
10	2.81×10^{-1}	2.55	1.37×10^{1}	2.35×10^{1}	8.90	2.04×10^{2}	1.59×10^{3}
100	3.93×10^{2}	3.57×10^{3}	1.91×10^{4}	3.28×10^{4}	1.20×10^{4}	2.00×10^{5}	6.99×10^{5}

Table 7
L_1^* relative position vector error e_r norm [km] over time t and for different degradation factor d, for Mylar.

t [days] ↓ / d→	0.01	0.1	1	10	100	1000	10000
1	1.14×10^{-4}	1.00×10^{-3}	5.37×10^{-3}	9.51×10^{-3}	4.67×10^{-3}	5.25×10^{-2}	6.05×10^{-1}
10	1.11×10^{-1}	1.00	5.40	9.55	4.69	5.08×10^{1}	4.65×10^{2}
100	1.55×10^{2}	1.41×10^{3}	7.57×10^{3}	1.34×10^{4}	6.51×10^{3}	5.46×10^{4}	2.42×10^{5}

Table 8
L_1^* relative velocity error e_v norm [km/s] over time t and for different degradation factor d, for Aluminum.

t [days] ↓ / d→	0.01	0.1	1	10	100	1000	10000
1	7.06×10^{-10}	6.41×10^{-9}	3.43×10^{-8}	5.77×10^{-8}	1.82×10^{-8}	7.01×10^{-7}	7.60×10^{-6}
10	7.11×10^{-8}	6.46×10^{-7}	3.46×10^{-6}	5.81×10^{-6}	1.84×10^{-6}	7.00×10^{-5}	7.07×10^{-4}
100	1.19×10^{-5}	1.08×10^{-4}	5.76×10^{-4}	9.68×10^{-4}	3.04×10^{-4}	1.09×10^{-2}	7.60×10^{-2}

minor variations of the heliocentric distance. Consequently, the associated temperature changes are expected to be sufficiently small to be neglected. For this reason, temperature-induced variations of the optical coefficients are not coupled to the orbital dynamics in the present simulations.

Finally, in the absence of degradation, the system would remain exactly at the equilibrium configuration. The degra-

Table 9
L_1^* relative velocity vector error e_v norm [km/s] over time t and for different degradation factor d, for CP1.

t [days] ↓ / d→	0.01	0.1	1	10	100	1000	10000
1	9.72×10^{-9}	8.83×10^{-8}	4.73×10^{-7}	8.13×10^{-7}	3.09×10^{-7}	7.46×10^{-6}	7.81×10^{-5}
10	9.79×10^{-7}	8.90×10^{-6}	4.77×10^{-5}	8.19×10^{-5}	3.10×10^{-5}	6.98×10^{-4}	4.92×10^{-3}
100	1.63×10^{-4}	1.48×10^{-3}	7.91×10^{-3}	1.35×10^{-2}	4.92×10^{-3}	7.69×10^{-2}	2.44×10^{-1}

Table 10
L_1^* relative velocity vector error e_v norm [km/s] over time t and for different degradation factor d, for Mylar.

t [days] ↓ / d→	0.01	0.1	1	10	100	1000	10000
1	3.82×10^{-9}	3.47×10^{-8}	1.87×10^{-7}	3.30×10^{-7}	1.62×10^{-7}	1.82×10^{-6}	2.08×10^{-5}
10	3.85×10^{-7}	3.50×10^{-6}	1.88×10^{-5}	3.33×10^{-5}	1.63×10^{-5}	1.75×10^{-4}	1.49×10^{-3}
100	6.41×10^{-5}	5.83×10^{-4}	3.13×10^{-3}	5.52×10^{-3}	2.69×10^{-3}	2.13×10^{-2}	8.55×10^{-2}

dation of the optical parameters modifies the effective solar-radiation-pressure force, producing a small displacement from the nominal equilibrium condition. This perturbation acts as a trigger for the naturally unstable dynamical modes of the system, which subsequently dominate the long-term drift of the trajectory.

An interesting feature can be observed in Fig. 6. Since the SRP acceleration decreases as the optical coefficients degrade, and since the initial attitude is defined by $\alpha = 0$, the initial perturbation is mainly aligned with the x $x+$ direction. From the equations of motion, this produces an initial negative acceleration contribution along x and a positive contribution along y. For values of d lower than approximately 100, this behaviour generally determines the escape direction during the first ~ 100 days.

However, when d is sufficiently large, the degradation-induced variation of the SRP acceleration becomes significant over a shorter time scale. Before the unstable modes fully dominate the dynamics, this larger acceleration mismatch can increase the velocity along y more rapidly. Through the coupling terms of the CR3BP equations, this also produces an increase of the positive acceleration along x. As a consequence, the trajectory trend changes and the sail initially escapes toward the positive x direction. At later times, the unstable modes become dominant again, the acceleration along x becomes positive and predominant, while the acceleration along y becomes negative. This explains the change in the escape trend from the neighbourhood of L_1^*.

The 3D trajectories are mainly intended to provide insight into the orbital regime experienced by a SSS when it is perturbed from L_1^*. From a dynamical perspective, the objective is to estimate the time required for the sunshade to reach the boundary of a region within which corrective manoeuvres can still steer the system back toward L_1^*. Up to about $t \simeq 100$ days, the sail gradually drifts away from L_1^* while remaining relatively close to its initial heliocentric distance. Beyond this time scale, the trajectory enters a different dynamical regime, where corrective manoeuvres may require excessive control effort. Moreover, some of the modelling assumptions, such as temperature-induced degradation and constant Λ, become less accurate because the heliocentric distance changes considerably over time.

Therefore, the relative errors e_r and e_v can be interpreted operationally. Once mission-specific limits on recoverable distance and velocity are defined according to the available actuators and control system, the contour plots and tables provide an estimate of the remaining time before the corrective manoeuvre becomes infeasible.

The same plots also highlight the change of escape trend occurring around $d \simeq 100$. In this region, the reversal of the acceleration trend produces values of the acceleration along x that remain close to zero for longer times. As a result, the position and velocity errors can temporarily decrease, keeping the trajectory closer to L_1^*. At later times, however, the unstable dynamics still lead to divergence. Similarly, for larger values of d, this temporary compensation effect becomes less relevant because the degradation-induced perturbation grows more rapidly.

In general, the magnitudes of e_r and e_v are only weakly affected by the choice of optical material. Nevertheless, as expected, larger values of Λ lead to faster divergence because the optical coefficients degrade more rapidly. For all three configurations, even a small perturbation of the SRP magnitude induced by degradation is sufficient to excite the intrinsic unstable modes of the three-body problem. These modes dominate the subsequent evolution and rapidly reduce the influence of small differences among the optical coefficients. Consequently, the initial drift away from L_1^* is triggered by degradation, but the long-term evolution is governed primarily by the underlying CR3BP dynamics.

For small values of d, the position error remains limited, while for larger values of d it can grow up to the order of 10^5 km. This behaviour is expected: the smaller the value of d, the weaker the degradation-induced SRP perturbation acting on the SSS around L_1^*, and therefore the longer the time required to significantly excite the unstable dynamical modes.

The material properties become relevant again when corrective control actions based on SRP are considered.

In this case, the maximum achievable control acceleration depends on the instantaneous values of the optical coefficients and therefore on the material-dependent degradation rate Λ_i. As a result, two sails that have experienced similar dynamical divergence may retain different control authority, directly affecting the feasibility and cost of recovery manoeuvres.

With respect to the classical model of Dachwald et al. (2006), shown in Figs. 12 and 13, the exponential degradation rate does not depend on the material and is generally larger than the material-dependent rates considered in this work. Consequently, the Dachwald model usually produces larger position and velocity errors, because the optical coefficients degrade faster. This difference is less evident only for small values of d or short propagation times, when the exponential degradation has not yet produced a significant deviation.

A similar behaviour is observed in Figs. 14–17. Since different values of Λ imply different degradation rates, the position and velocity errors evolve at different speeds over time. Quantitatively, these plots show how the maximum position and velocity errors vary with t and d when an uncertainty of $\pm 50\%$ is assumed on Λ. The effect is more pronounced for large values of d and for propagation times longer than approximately 10 days.

In all the difference plots, the same qualitative pattern around $d \simeq 100$ is preserved. This confirms that the change in the escape trend is not an artefact of a specific material choice or degradation-rate assumption, but is instead associated with the coupled effect of SRP degradation and the local unstable dynamics around L_1^*.

6. Conclusions and future works

In this work, a degradation model for solar sail optical properties has been developed to account for different radiation sources and to study their dependence on temperature. At L_1, solar sail materials are exposed to the full spectrum of solar electromagnetic radiation and to high-energy elementary particles, leading to a degradation of their optical and thermal properties. In particular, for the radiation-induced degradation, the reflectivity of the sail, which is the parameter that most significantly affects orbital motion, will degrade over time. This temporal variation is modeled as an exponential decay law, with a degradation rate that depends on α-particles, protons, UV radiation, and γ radiation, and that varies based on the materials employed. In the present work, Aluminium, CP1, and Mylar are considered for simulations. For temperature-induced degradation, for the three materials considered, the operational temperature at the heliocentric distance relevant to the sunshade application remains in the range of 300 K to 600 K. However, when taking into account the radiation-induce degradation, an increase in the sail material temperature is observed. Since the material reflectivity has been shown to remain nearly constant within this range, the degradation model solely accounts for radiation-induced degradation.

By integrating this degradation model within the Photogravitational Circular Restricted Three Body Problem, we have assessed how time-varying optical coefficients modify the dynamical environment and influence the behavior of Solar-Sail Satellites operating in non-Keplerian orbits around the Sun–Earth/Moon's System Center of Mass. Overall, the results indicate that firstly the loss of accuracy around the L_1^* point is given by the optical coefficients degradation which acts as a trigger, but then is driven mainly by the intrinsic instability of the dynamics, largely independent of the specific sail material; then, secondly, the choice of sail material, via its degradation rate Λ_i, has a critical impact on the time-scale of degradation and so the available Solar Radiation Pressure control authority and on the feasibility of recovery strategies, even when the uncontrolled dynamical evolution appears qualitatively similar.

The findings are of great importance for the Planetary Sunshade Program, where a swarm of Solar-Sail Satellites will operate over extended period of time. For such missions, maintaining the designed position is essential both to meet the climate requirements and to guarantee the overall swarm stability. Neglecting degradation effects may lead to reduced control authority and, ultimately, to the loss of the desired orbital configuration. Future developments should focus on refining the degradation model, in particular through experimental characterization, and direct in-space testing necessary to validate degradation models under real environmental conditions.

Declaration of competing interest

The authors declare that they have no known competing financial interests or personal relationships that could have appeared to influence the work reported in this paper.

Acknowledgments

M. C. was supported within PNRR-NGEU project, funded by MUR - DM 118/2023 and R. Ya. K. was supported by the City University of New York PSC CUNY Research Grant No. 68298–0046.

Appendix A. Derivatives

Let us define with γ as the generic variable $[x, y, z]$ where derivatives are calculated with respect to.

A.1. Position vector $r_{1,2}$

The components matrices in S-CCS of vector derivatives $(r_{1,2})_\gamma$ are given by direct derivation from Eq. (8) as

$$(\boldsymbol{r}_{1,2})_\gamma = \begin{bmatrix} \left(r^x_{1,2}\right)_\gamma \\ \left(r^y_{1,2}\right)_\gamma \\ \left(r^z_{1,2}\right)_\gamma \end{bmatrix} = \begin{bmatrix} x_\gamma \\ y_\gamma \\ z_\gamma \end{bmatrix}, \tag{45}$$

with

$$\begin{aligned} (\boldsymbol{r}_{1,2})_x &= \begin{bmatrix} 1 \\ 0 \\ 0 \end{bmatrix}, \\ (\boldsymbol{r}_{1,2})_y &= \begin{bmatrix} 0 \\ 1 \\ 0 \end{bmatrix}, \\ (\boldsymbol{r}_{1,2})_z &= \begin{bmatrix} 0 \\ 0 \\ 1 \end{bmatrix}. \end{aligned} \tag{46}$$

Furthermore, the norm derivative $(\|\underline{r}_{1,2}\|)_\gamma$ is given by direct derivation from Eqs. (8) and (4) as

$$\begin{aligned} (\|\underline{r}_1\|)_\gamma &= \frac{(x+\mu)x_\gamma + yy_\gamma + zz_\gamma}{\|\underline{r}_1\|}, \\ (\|\underline{r}_2\|)_\gamma &= \frac{(x-1+\mu)x_\gamma + yy_\gamma + zz_\gamma}{\|\underline{r}_1\|}, \end{aligned} \tag{47}$$

with

$$\begin{aligned} (\|\underline{r}_1\|)_x &= \frac{x+\mu}{\|\underline{r}_1\|}, \quad (\|\underline{r}_2\|)_x = \frac{x-1+\mu}{\|\underline{r}_2\|}, \\ (\|\underline{r}_{1,2}\|)_y &= \frac{y}{\|\underline{r}_{1,2}\|}, \\ (\|\underline{r}_{1,2}\|)_z &= \frac{z}{\|\underline{r}_{1,2}\|}. \end{aligned} \tag{48}$$

A.2. CR3BP potential U

The derivative U_γ is given by direct derivation from Eq. (10) as

$$U_\gamma = xx_\gamma + yy_\gamma - (1-\mu)\frac{(\|\underline{r}_1\|)_\gamma}{\|\underline{r}_1\|^2} - \mu\frac{(\|\underline{r}_2\|)_\gamma}{\|\underline{r}_2\|^2} \tag{49}$$

with

$$\begin{aligned} U_x &= x - (1-\mu)\frac{x+\mu}{\|\underline{r}_1\|^3} - \mu\frac{x-1+\mu}{\|\underline{r}_2\|^3}, \\ U_y &= y\left(1 - \frac{1-\mu}{\|\underline{r}_1\|^3} - \frac{\mu}{\|\underline{r}_2\|^3}\right), \\ U_z &= z\left(-\frac{1-\mu}{\|\underline{r}_1\|^3} - \frac{\mu}{\|\underline{r}_2\|^3}\right). \end{aligned} \tag{50}$$

References

Ancona, E., Kezerashvili, R.Ya., 2017. Temperature restrictions for materials used in aerospace industry for the near-sun orbits. Acta Astronaut. 140, 565–569. https://doi.org/10.1016/j.actaastro.2017.09.002.

Ancona, E., Kezerashvili, R.Ya., 2019. Extrasolar space exploration by a solar sail accelerated via thermal desorption of coating. Adv. Space Res. 63 (7), 2021–2034. https://doi.org/10.1016/j.asr.2018.12.016.

Ancona, E., Kezerashvili, R.Ya., 2025. Recent advances in space sailing missions and technology: review of the 6th international symposium on space sailing (ISSS 2023). Aeronaut. Aerospace Open Access J. 9 (1), 62–73. https://doi.org/10.15406/aaoaj.2025.09.00221.

ASTM International, 2023. Astm g173–23: Standard tables for reference solar spectral irradiances: direct normal and hemispherical on 37° tilted surface. URL: https://www.astm.org/g0173-23.html.

Bassetto, M., Quarta, A.A., Mengali, G., et al., 2020. Trajectory analysis of a sun-facing solar sail with optical degradation. J. Guid., Control, Dynam. 43 (9), 1727–1732. https://doi.org/10.2514/1.G005214.

Baum, C.M., Low, S., Sovacool, B.K., 2022. Between the sun and us: expert perceptions on the innovation, policy, and deep uncertainties of space-based solar geoengineering. Renew. Sustain. Energy Rev. 158, 112179. https://doi.org/10.1016/j.rser.2021.112179.

Betts, B., Brinza, D., Vaughn, J., et al., 2021. Lightsail 2: controlled solar sailing using a cubesat. Nat. Astron. 5, 18–25. https://doi.org/10.1038/s41550-020-01264-1.

Chesley, B., Matonti, C.L., Sonty, S.S., et al., 2023. A conceptual framework for climate change mitigation actions employing in-space geoengineering. In: 74th International Astronautical Congress. IAF, Baku, AZ.

Coco, M., Matonti, C.L., Cappelletti, C. et al., 2025. Planetary sunshade for solar geoengineering: preliminary design of a precursor system and mission. Acta Astronaut., 235, 452–462. URL: https://www.sciencedirect.com/science/article/pii/S0094576525003133. doi:10.1016/j.actaastro.2025.05.031.

Dachwald, B., Mengali, G., Quarta, A., et al., 2006. Parametric model and optimal control of solar sails with optical degradation. J. Guid., Control, Dynam. 29, 1170–1178. https://doi.org/10.2514/1.20313.

Dachwald, B., Seboldt, W., Macdonald, M., et al., 2005. Potential solar sail degradation effects on trajectory and attitude control. In: AIAA guidance, navigation, and control conference and exhibit, p. 6172. https://doi.org/10.2514/6.2005-6172.

DuPont, 2013. Dupont CP1 Technical Data Sheet. https://www.dupont.com. Accessed from manufacturer documentation.

Edwards, D.L., Hubbs, W., Stanaland, T. et al., 2002. Characterization of space environmental effects on candidate solar sail material. In: Photonics for Space Environments VIII (pp. 67–74). SPIE volume 4823. doi:10.1117/12.451455.

Edwards, D.L., Hubbs, W.S., Wertz, G.E., et al., 2004a. Electron radiation effects on candidate solar sail material. High Perform. Polym. 16 (2), 277–288. https://doi.org/10.1177/0954008304044106.

Edwards, D.L., Semmel, C., Hovater, M., et al., 2006. Status of solar sail material characterization at NASA's Marshall Space Flight Center. In: Protection of materials and structures from the space environment. Springer, pp. 233–246. https://doi.org/10.1007/1-4020-4319-8_22.

Edwards, D.L., Semmel, C., Hovater, M.A. et al., 2004b. Solar sail material performance property response to space environmental effects. In: Photonics for Space Environments IX (pp. 80–91). SPIE volume 5554. doi:10.1117/12.562809.

European Cooperation for Space Standardization (ECSS), 2019. Space Engineering: Spacecraft Charging. Technical Report ECSS-E-ST-20-06C Rev. 1 ECSS.

European Space Agency (ESA), 2015. Thermal Control Handbook for Spacecraft and Instruments. Noordwijk, The Netherlands.

Fuglesang, C., de Herreros Miciano, M., 2021. Realistic sunshade system at L1 for global temperature control. Acta Astronaut., 186, 269–279. URL: https://www.sciencedirect.com/science/article/pii/S0094576521001995. doi:10.1016/j.actaastro.2021.04.035.

Govindasamy, B., Caldeira, K., 2000. Geoengineering Earth's radiation balance to mitigate CO2-induced climate change. Geophys. Res. Lett. 27 (14), 2141–2144. https://doi.org/10.1029/1999GL006086.

Hanks, C.L., Hamman, D.J., 1971. Radiation Effects Design Handbook: Section 3 – Electrical Insulating Materials and Capacitors. Technical Report NASA CR-1787 NASA., URL: https://ntrsnasa.gov/api/citations/19710020300/downloads/19710020300.pdf.

Heaton, A.F., Artusio-Glimpse, A.B., 2015. An Update to the NASA Reference Solar Sail Thrust Model. Technical Report NASA/TP–2015–218894 NASA Marshall Space Flight Center. URL: https://

ntrs.nasa.gov/citations/20150021404. doi:10.2514/6.2015-4506 NASA Technical Publication.

Huang, J., Biggs, J.D., Bai, Y. et al., 2021a. Integrated guidance and control for solar sail station-keeping with optical degradation. Adv. Space Res., 67(9), 2823–2833. URL: https://www.sciencedirect.com/science/article/pii/S0273117720300284. doi:10.1016/j.asr.2020.01.010. Solar Sailing: Concepts, Technology, and Missions II.

Huang, X., Zeng, X., Circi, C. et al., 2021b. Analysis of the solar sail deformation based on the point cloud method. Adv. Space Res., 67(9), 2613–2627. URL: https://www.sciencedirect.com/science/article/pii/S0273117720303318. doi:10.1016/j.asr.2020.05.008. Solar Sailing: Concepts, Technology, and Missions II.

Jehle, A., Scott, E., Centers, R., 2020. A planetary sunshade built from space resources. ASCEND. Virtual Event. https://doi.org/10.2514/6.2020-4077.

Johnson, L., Betts, B., Bellardo, J., et al., 2016. Lightsail program: demonstration of controlled solar sailing in cubesat form. Adv. Space Res. 57 (11), 2486–2494. https://doi.org/10.1016/j.asr.2016.02.006.

Kang, J.H., Bryant, R.G., Wilkie, W.K., et al., 2017. Simulated Space Environment Effects on a Candidate Solar Sail Material. NASA Technical Report NASA/TP-2017-219644. NASA Langley Research Center.

Kezerashvili, R. Ya., 2009. Thickness requirement for solar sail foils. Acta Astronaut., 65(3), 507–518. URL: https://www.sciencedirect.com/science/article/pii/S0094576509000939. doi:10.1016/j.actaastro.2009.01.062.

Kezerashvili, R.Ya., 2014. Solar sail: Materials and space environmental effects. In: Macdonald, M. (Ed.), Advances in Solar Sailing Springer Praxis Books. Springer, Berlin, Heidelberg, pp. 573–592. https://doi.org/10.1007/978-3-642-34907-2_25.

Kezerashvili, R.Ya., Matloff, G.L., 2007. Solar radiation and the beryllium hollow-body sail: 1. The ionization and disintegration effects. J. Brit. Interplanet. Soc. 60, 169–179.

Kezerashvili, R. Ya., Matloff, G.L., 2009. Microscopic approach to analyze solar-sail space-environment effects. Adv. Space Res., 44(7), 859–869. URL: https://www.sciencedirect.com/science/article/pii/S0273117709003445. doi:10.1016/j.asr.2009.05.002.

Kleiman, J., Tennyson, R.C., 1999. Protection of Materials and Structures from the Low Earth Orbit Space Environment: Proceedings of ICPMSE-3, Third International Space Conference, held in Toronto. Springer Science & Business Media, Canada.

Klein, E.M., Seefeldt, P., Sznajder, M., et al., 2026. Solar sail propulsion limitations due to hydrogen blistering: progression of reflectance decrease. Adv. Space Res., In Press. https://doi.org/10.1016/j.asr.2025.12.061.

Kudaikulova, S.K., Iskakov, R., Vecherkina, E., et al., 2008. New metalized polyimide films structure and physical properties. Open Chem. Eng. J. 2, 66–72. https://doi.org/10.2174/1874123100802010066.

Lebedev, P.N., 1901. First experimental evidence for pressure of the light on solid bodies. Ann. Phys. 6, 433–458.

Lichodziejewski, D., West, J., Reinert, R., et al., 2004. Development and ground testing of a compactly stowed inflatably deployed solar sail. In: 45th AIAA/ASME/ASCE/AHS/ASC Structures, Structural Dynamics & Materials Conference, p. 1507. https://doi.org/10.2514/6.2004-1507.

Loke, S., Naqavi, A., Warmann, E., et al., 2022. Ultra-lightweight mirrors with high solar reflectivity and high infrared emissivity for sun-facing radiative thermal management in space. Opt. Exp. 30 (16), 28268–28278. https://doi.org/10.1364/OE.454212.

Lu, T., Solis-Ramos, E., Yi, Y. et al., 2018. UV degradation model for polymers and polymer matrix composites. Polym. Degrad. Stabil., 154, 203–210. URL: https://www.sciencedirect.com/science/article/pii/S0141391018301964. doi:10.1016/j.polymdegradstab.2018.06.004.

Maraveas, C., Kyrtopoulos, I.V., Arvanitis, K.G. et al., 2024. The aging of polymers under electromagnetic radiation. Polymers, 16(5). URL: https://www.mdpi.com/2073-4360/16/5/689. doi:10.3390/polym16050689.

Matonti, C.L., Apa, R., Romano, M., 2023a. New results on the mass-optimization analysis of a planetary sunshade system. In: 74th International Astronautical Congress. IAF, Baku, AZ.

Matonti, C.L., Coco, M., Cappelletti, C., et al., 2026. Roadmap toward a planetary sunshade for space-based solar geoengineering. Adv. Space Res., In Press. https://doi.org/10.1016/j.asr.2026.04.007.

Matonti, C.L., Manuri, F., Romano, M., 2025. Extended reality for space and astronautical engineering applications. In: 76th International Astronautical Congress. IAF, Sydney, AU.

Matonti, C.L., Romano, M., 2024. New families of halo orbits about the photo-gravitational equilibrium in the Sun - Earth/Moon system's center of mass elliptic restricted three body problem for planetary sunshade missions. In: 75th International Astronautical Congress. IAF, Milano, IT.

Matonti, C.L., Scantamburlo, E., Romano, M., 2023b. New families of halo orbits about the photo-gravitational equilibrium between Sun and the Earth/Moon system for planetary sunshade missions. In: 74th International Astronautical Congress. IAF, Baku, AZ.

Maxwell, J.C., 1865. A dynamical theory of the electromagnetic field. Philos. Trans. Roy. Soc. London, 155, 459. CLV.

Maxwell, J.C., 1873. A Treatise on Electricity and Magnetism. Oxford University Press, Oxford.

McInnes, C., 2010. Space-based geoengineering: challenges and requirements. J. Mech. Eng. Sci. 224, 571–580. https://doi.org/10.1243/09544062JMES1439.

McInnes, C.R., 1999. Solar Sailing: Technology, Dynamics and Mission Applications. Springer, Berlin.

McInnes, C.R., 2014. Approximate closed-form solution for solar sail spiral trajectories with sail degradation. J. Guid., Control, Dynam. 37 (6), 2053–2057. https://doi.org/10.2514/1.G000225.

McKay, R.J., Macdonald, M., Biggs, J., et al., 2011. Survey of highly non-keplerian orbits with low-thrust propulsion. J. Guid., Control, Dynam. 34 (3), 645–666. https://doi.org/10.2514/1.52133.

Mengali, G., Quarta, A.A., Circi, C., et al., 2007. Refined solar sail force model with mission application. J. Guid., Control, Dynam. 30 (2), 512–520. https://doi.org/10.2514/1.24779.

Modest, M.F., 2013. Radiative Heat Transfer, 3rd ed. Academic Press, Oxford.

National Aeronautics and Space Administration (NASA), 1972. Radiative Properties of Materials Used in Spacecraft. Technical Report NASA-TN-D-7080 NASA Washington, DC.

National Aeronautics and Space Administration (NASA), Science Mission Directorate (2024). Ultraviolet waves. https://science.nasa.gov/ems/10_ultravioletwaves/. Accessed: 2025-06-26.

Nehls, M., 2005. CP1 Environmental Effects Testing. Technical Report MSFC-TR-2005 NASA Marshall Space Flight Center. NASA Technical Report.

Niccolai, L., Quarta, A.A., Mengali, G., 2022. Trajectory approximation of a solar sail with constant pitch angle and optical degradation. IEEE Trans. Aerosp. Electron. Syst. 58 (4), 3643–3649. https://doi.org/10.1109/TAES.2021.3124867.

Nichols, R.F., Hull, G.F., 1903. Pressure due to radiation. Phys. Rev. (Ser. I) 17, 26–50.

Oggionni, F., Heiligers, J., Sánchez Cuartielles, J., 2022. Trajectory optimization of a planetary sunshade around the Sun-Earth L_1 point for solar geoengineering. ASCEND 2022. https://doi.org/10.2514/6.2022-4388.

Parker, W.J., Abbott, G.L., 1965. Theoretical and experimental studies of the total emittance of metals. In: Symposium on Thermal Radiation of Solids NASA SP-55 (pp. 11–28). NASA.

Perelman, Y.M., 1915. Mezhplanetnie puteshestvia (Interplanetary Journeys). P.P. Soykin, Peterburg, In Russian.

Polyakhova, E., 1986. Kosmicheskii polet s solnechnim parusom (Space Solar Sailing). Nauka, Moscow, In Russian.

Prosvirikov, V., Grigorevskiy, A., Kiseleva, L., et al., 2006. Influence of space environment on spectral optical properties of thermal control coatings. In: Protection of Materials and Structures from the Space

Environment. Springer, pp. 61–69. https://doi.org/10.1007/1-4020-4319-8_7.

Roger, A., 2006. Feasibility of cooling the Earth with a cloud of small spacecraft near the inner Lagrange point (L1). Proc. Natl. Acad. Sci. (PNAS) 103 (46), 17184–17189. https://doi.org/10.1073/pnas.0608163103.

Romano, M., Chesley, B., Matonti, C.L., et al., 2023. Survey and comparison of in-space and in-atmosphere geo-engineering concepts for climate change mitigation. In Global Space Conference on Climate Change. IAF, Oslo, NO.

Ross, S., Koon, W., Lo, M., et al., 2022. Dynamical Systems, the Three-Body Problem and Space Mission Design. Marsden Books.

Rottman, G., 2005. The SORCE mission. Sol. Phys. 230, 7–25. https://doi.org/10.1007/s11207-005-8112-6.

Rozhkov, M.A., Starinova, O.L., Chernyakina, I.V., 2021. Influence of optical parameters on a solar sail motion. Adv. Space Res., 67(9), 2757–2766. URL: https://www.sciencedirect.com/science/article/pii/S0273117720304191. doi:10.1016/j.asr.2020.06.017.

Shen, Z., Xia, Y., Zhao, C. et al., 2020. Degradation mechanism of polyimide film irradiated by gamma ray. In: Journal of Physics: Conference Series (p. 012026). volume 1622. doi:10.1088/1742-6596/1622/1/012026.

Szebehely, V., 1967. Theory of Orbits, the Restricted Problem of Three Bodies. Academic Press.

Sznajder, M., Geppert, U., Dudek, M., 2015. Degradation of metallic surfaces under space conditions, with particular emphasis on hydrogen recombination processes. Adv. Space Res. 56, 71–84. https://doi.org/10.1016/j.asr.2015.03.032.

Sznajder, M., Geppert, U., Dudek, M.R., 2018. Hydrogen blistering under extreme radiation conditions. npj Mater. Degrad. 2, 1–8. https://doi.org/10.1038/s41529-017-0024-z.

Sznajder, M., Seefeldt, P., Sprow¨itz, T., et al., 2020. Solar sail propulsion limitations due to hydrogen blistering. Adv. Space Res. 67, 2655–2668. https://doi.org/10.1016/j.asr.2020.06.034.

Sánchez, J., McInnes, C., 2015. Optimal sunshade configurations for space-based geoengineering near the Sun-Earth L1 point. PLOS ONE 10. https://doi.org/10.1371/journal.pone.0136648.

Touloukian, Y.S., DeWitt, D.P., 1972. Thermophysical properties of matter-the TPRC data series. Volume 8. Nonmetallic Solids.

Tsander, F.A., 1967. Iz nauchnogo nasledia (From a Scientific Heritage). Nauka, Moscow, In Russian.

Tsander, F.A., 1977. Selected Papers. Zinatne, Riga, In Russian.

Tsiolkovsky, K.E., 1921. Extension of man into outer space volume 2.

United Nations, 2026. The 17 goals. URL: https://sdgs.un.org/goals accessed: 2026-04-25.

Vulpetti, G., Apponi, D., Zeng, X. et al., 2021. Wrinkling analysis of solar-photon sails. Adv. Space Res., 67(9), 2669–2687. URL: https://www.sciencedirect.com/science/article/pii/S0273117720304932. doi:10.1016/j.asr.2020.07.016. Solar Sailing: Concepts, Technology, and Missions II.

Vulpetti, G., Scaglione, S., 1999. The aurora project: Estimation of the optical sail parameters. Acta Astronaut., 44(2), 123–132. URL: https://www.sciencedirect.com/science/article/pii/S0094576599000387. doi:10.1016/S0094-5765(99)00038-7. Missions to the Outer Solar System and Beyond.

Williams, D.R., 2024. Planetary fact sheets. URL: https://nssdc.gsfc.nasa.gov/planetary/planetfact.html.

Zou, J., Li, D., Wang, J., et al., 2022. Experimental study of measuring the wrinkle of solar sails. Aerospace 9, 289. https://doi.org/10.3390/aerospace9060289.